Study of Strontium Titanate and Barium Zirconate Properties Using Molecular Dynamics Simulation

by

Goh Wen Fong

Thesis submitted in fulfillment

of the requirements for the degree of

Master of Science

April 2013

"Imagination is more important than knowledge. For knowledge is limited, whereas imagination embraces the entire world, stimulating progress, giving birth to evolution."

Albert Einstein

Acknowledgements

I would like to express my gratitude to all the people who helped me in this research. This work could not have been accomplished without the help of these people.

First, I would like to thank Assoc. Prof. Dr. Sohail Aziz Khan for his useful advice and suggestions during the progress of the study. The papers could not have been published without his help. His advice and contribution towards successful completion of this work are highly appreciated.

Second, I am grateful to Dr. Yoon Tiem Leong for providing me a pleasant and tranquil workplace, in which I regarded as one of the most important factors to succeed.

Third, I would like to thank my family and my friends for their constant supports and understandings. Special thanks goes to Ms. Ching Chin Peng, for her help, support, motivation and encouragement throughout the study.

Lastly, I would like to acknowledge the support from the USM Fellowship.

Contents

List of Tables

List of Figures

Abbreviations

$BaZrO_3$	**B**arium **Z**irconate
$SrTiO_3$	**S**trontium **T**itanate
MD	**M**olecular **D**ynamics
NEMD	**N**on-**E**quilibrium **M**olecular **D**ynamics
SC	**S**imple **C**ubic
BCC	**B**ody-**C**entered **C**ubic
FCC	**F**ace-**C**entered **C**ubic
DNA	**D**eoxyribo**N**ucleic **A**cid

Physical Constants

Boltzmann Constant	k_B	=	$1.3806503 \times 10^{-23}$ m^2 kg s^{-2} K^{-1}
Gas Constant	R	=	8.314472 J mol^{-1} K^{-1}
Planck Constant	$\hbar$	=	1.054572×10^{-34} m^2 kg s^{-1}
Coulomb Constant	k_e	=	8.987552×10^{9} N m^2 C^{-2}
Avogadro constant	N_A	=	6.022142×10^{23} mol^{-1}
Force Constant	f_0	=	1.0 kcal Å^{-1} mol^{-1}

Symbols

r	interatomic seperation	Å
q	coulomb charge	e
σ	ionic radii	Å
ρ	ionic softness	Å
C	Van der Waals attraction parameter	$\text{kcal}^{\frac{1}{2}}$ Å^3 $\text{mol}^{-\frac{1}{2}}$
D	potential well depth	kcal mol^{-1}
Ω	potential steepness	Å^{-1}
r_0	equilibrium distance	Å
δt	time step	s
r_c	cut-off distance	Å
T	temperature	K
P	pressure	Pa or atm
E	total energy	kcal (1 kcal = 4184 J)
K	kinetic energy	kcal
U	potential energy	kcal
H	enthalpy	kcal
t	time	s
J	heat flux	W m^{-2}
L	length of simulation cell	Å or unit cell

a	lattice constant	Å
b	lattice constant	Å
c	lattice constant	Å
A	angle	° (deg)
B	angle	° (deg)
Γ	angle	° (deg)
ϱ	density	kg m^{-3}
V	molar volume	m^3 mol^{-1}
α	linear thermal expansion coefficient	K^{-1}
β_T	isothermal compressibility	Pa^{-1}
C_P	heat capacity at constant pressure	J mol^{-1} K^{-1}
κ	thermal conductivity	W m^{-1} K^{-1}

KAJIAN TENTANG STRONTIUM TITANAT DAN BARIUM ZIRCONAT DENGAN MENGGUNAKAN SIMULASI DINAMIK MOLEKUL

ABSTRAK

Simulasi dinamik molekul telah dijalankan ke atas bahan-bahan perovskit strontium titanat dan barium zirkonat dalam usaha untuk mengkaji tingkahlaku atom mikroskopik, dan termodinamik makroskopik serta sifat-sifat pengangkutan haba mereka. Keupayaan rumit atom boleh dipermudahkan kepada interaksi berpasangan yang terdiri daripada interaksi ionik, tolakan jarak dekat, tarikan Van der Waals dan ikatan kovalen Morse. Set parameter-parameter keupayaan strontium titanat dan barium zirkonat yang baru telah diperolehi. Fungsi penaburan jejarian telah diperolehi untuk mengkaji tingkahlaku atomik dan strukturnya. Parameter-parameter struktur, pekali pengembangan terma, kebolehmampatan sesuhu, kapasiti haba dan konduktiviti haba telah dinilai dalam lingkungan suhu 298 - 2000 K dan tekanan daripada 1 atm kepada 20.3 GPa. Pada suhu bilik, nilai-nilai parameter kekisi strontium titanat and barium zirkonat adalah 3.9051 Å dan 4.1916 Å. Pengiraan pekali pengembangan haba strontium titanat and barium zirkonat memberi nilai 1.010 $\times 10^{-5}\mathrm{K}^{-1}$ dan 0.816 $\times 10^{-5}\mathrm{K}^{-1}$ pada 298 K, manakala pengiraan kebolehmampatan sesuhu memberi nilai 5.800 $\times 10^{-12}\mathrm{Pa}^{-1}$ kepada strontium titanat dan 7.338 $\times$ 10^{-12} Pa^{-1} kepada barium zirkonat. Kapasiti haba strontium titanat and barium zirkonat adalah 126.8 J mol^{-1} K^{-1}

dan 110.8 J mol^{-1} K^{-1} pada suhu bilik. Pengiraan kekonduksian terma telah dilakukan dengan menggunakan kaedah dinamik molekul tak-seimbang, dan pembetulan kepada kesan saiz telah dilakukan. Peda suhu bilik, nilai-nilai konduktiviti haba strontium titanat and barium zirkonat adalah 11.04 W m^{-1} K^{-1} dan 4.263 W m^{-1} K^{-1}. Keputusan-keputusan simulasi memperlihatkan persetujuan yang baik dengan penemuan-penemuan eksperimen.

STUDY OF STRONTIUM TITANATE AND BARIUM ZIRCONATE PROPERTIES USING MOLECULAR DYNAMICS SIMULATION

ABSTRACT

Molecular dynamics simulation has been carried out on strontium titanate and barium zirconate in order to study the microscopic atomic behavior, and the macroscopic thermodynamic and thermal transport properties of the perovskite materials. The intricate interatomic potentials can be simplified into pairwise interactions, which consist of ionic interaction, short-range repulsion, Van der Waals attraction and Morse covalent bonding. New sets of potential parameters of strontium titanate and barium zirconate have been presented. Radial distribution functions have been obtained to study the atomic and structural behavior. Structural parameters, thermal expansion coefficient, isothermal compressibility, heat capacity and thermal conductivity have been evaluated in the temperature range of 298 - 2000 K and pressure ranging from 1 atm to 20.3 GPa. At room temperature, the values of lattice parameters of strontium titanate and barium zirconate are obtained to be 3.9051 Å and 4.1916 Å. While the calculation of thermal expansion coefficients of strontium titanate and barium zirconate gives 1.010 $\times 10^{-5} K^{-1}$ and 0.816 $\times 10^{-5} K^{-1}$ at 298 K, the isothermal compressibility of the materials yields 5.800 $\times 10^{-12} Pa^{-1}$ for strontium titanate and 7.338 $\times$ 10^{-12} Pa^{-1} for barium zirconate. The heat capacity of strontium titanate and barium zirconate are calculated to be 126.8 J mol^{-1} K^{-1} and 110.8 J mol^{-1} K^{-1} at

room temperature. Thermal conductivity calculation was performed using non-equilibrium molecular dynamics method, and correction for finite size effects has been made. At room temperature, the values of thermal conductivities are obtained to be 11.04 W m^{-1} K^{-1} for strontium titanate and 4.263 W m^{-1} K^{-1} for barium zirconate. The simulation results show good agreement with the experimental findings.

Chapter 1

Introduction

For development of technology and to meet new demands of tomorrow's society, there is a constant need for new materials with new or improved properties. Compounds with perovskite structure have shown many intriguing properties, such as ferroelectricity, high temperature superconductivity, high dielectric constant, piezoelectricity, thermoelectricity, etc. These properties make the perovskite compounds a suitable functional materials for applications in many areas. For example, barium titanate $BaTiO_3$ can be used to produce ferroelectric memories in constrast to the conventional dielectric memories, and lead zirconate titanate $Pb(Zr_xTi_{1-x})O_3$ $(0 \leq x \leq 1)$ or simply PZT can be used to manufacture piezoelectric transducers. Therefore these materials will continue to attract great interest. Despite the fact that there are tons of perovskite materials that show interesting properties and useful applications, particular interest has been given to strontium titanate $SrTiO_3$ and barium zirconate $BaZrO_3$ ceramic materials in this study.

$SrTiO_3$, which is one of the most common ceramic materials, possesses an ideal cubic perovskite structure with lattice constant of 3.9051 Å [2] and space group of

$Pm\bar{3}m$ at room temperature. Below 105 K, it is in a ferroelectric phase [3]. This perovskite material finds useful applications, among other things, in electronics and electrical insulations. Furthermore, it has been shown by some researchers that its electrical, thermal and thermoelectric properties can be greatly modified by introducing oxide defects or doped with alkaline earth metals or transition metals. For instance, niobium-doped strontium titanate can be electrically conductive [4], lanthanum-doped strontium titanate is a promising thermoelectric material [5, 6] and cerium-doped strontium titanate can be used in fuel cells applications [7].

On the other hand, $BaZrO_3$, which has a cubic perovskite structure with lattice constant of 4.192 Å [8] and space group of $Pm\bar{3}m$ at room temperature, is one of the most useful ceramic materials. Since it is stable with the paraelectric cubic structure, it does not show phase transition with temperature [9]. This perovskite material has a wide range of applications, including thermal barrier coating [10], nuclear fuel [11], refractory [12] and protonic ceramic fuel cell [13].

Since some of the devices made from these materials operate at high temperature and high pressure, it is important to understand the physical properties and stabilities of the materials at these extreme conditions. However, performing experiments at these extreme conditions can be costly or difficult or even impossible due to practical limitations. Conversely, computer simulations provide an alternative route to evaluate the materials' physical properties at these extreme cases. Computer simulations are not only useful to investigate the materials' macroscopic behavior, they are also powerful to study materials from the microscopic point of view, such as obtaining the atomic structure, which is usually done by using x-ray diffraction method.

Molecular dynamics simulation, which belongs to one of the two main families of computer simulations (the other one is Monte Carlo simulation), has been a promising tool for study of various kind of materials, from simple crystalline structures, such as solid argon [14], to complex bio-molecular structures, such as proteins [15] and DNA [16]. Just to mention some, molecular dynamics method has been used to study thermal-physical properties of alkali nitrate salts [17], rare-earth zirconates [18], magnesium silicate $MgSiO_3$ perovskite [19, 20], $Bi_{2.5}Na_{1.5}Nb_3O_{12}$ compounds [21], neptunium dioxide NpO_2 [22], uranium dioxide UO_2 [23] and carbon nanotubes [24, 25]. The potentials used in molecular dynamics simulations have also been formulated from a simple Lennard-Jones pairwise potential into much involved potentials, such as embedded-atom method (EAM) potentials for metals and metal alloys [26, 27], reactive force-field for hydrocarbons [28], three-body potential [29, 30], etc. Furthermore, the techniques have also been improved to couple with genetic algorithm [31, 32] and ab-initio method [33].

In this study, molecular dynamics simulations have been carried out to understand the thermodynamic and thermal transport properties of $SrTiO_3$ and $BaZrO_3$ perovskite materials in the temperature range of $298 - 2000$ K and pressure range from 1 atm to 20.3 GPa. Due to the fact that some of the potential parameters found in the literature cannot reproduce some of the properties, new and more accurate sets of potential parameters of $SrTiO_3$ and $BaZrO_3$ have been derived. Using our own derived potential parameters, we would like to explore the possibility of obtaining the structural parameters, thermal expansion coefficient, isothermal compressibility, heat capacity and thermal conductivity of the compounds. Furthermore, using molecular dynamics simulations, we hope to

enhance our understanding on the perovskite materials not only from the macroscopic point of view, but also the physics behind the macroscopic properties. In addition, we would like to obtain the relation between the atomic behavior and the observed macroscopic properties. In order to obtain good predictions of the macroscopic physical properties, one of the criteria is that the interatomic interactions must be described correctly. Correctness of the simulation results can be gauged by comparing against the experimental data. Moreover, it is hoped that this study could serve as a reference to researchers using molecular dynamics simulation to perform similar calculations on other materials.

In summary, the aim of this research is to:

- Derive more accurate sets of potential parameters of strontium titanate and barium zirconate.
- Obtain the variations of structural parameters, thermal expansion coefficient, isothermal compressibility, heat capacity and thermal conductivity of the perovskites with temperature and pressure.
- Study the radial distribution functions of the materials.
- Compare the simulation results against the experimental findings.

The thesis is organized is such a way that after theories of solid state physics and molecular dynamics are introduced, methodology of the research is described and follow by results and discussions. Lastly, conclusions are made and some recommendations for futher study are proposed.

Chapter 2

Background Theory I - Solid State Physics

Solid state physics, which is the largest branch of condensed matter physics, is one of the fundamental studies in physics. It is a study that covers every aspects related to crystalline materials, or rather, it is a study of macroscopic properties of crystalline materials which results from their constituent microscopic bahavior. Since the invention of the transistor, where smaller and lighter electronic devices are made possible, solid state physics has become a very important field of study. For example, the computers in the past were as huge as a room, but nowadays, the computers are much smaller that they are able to be fit into a workspace, or even carry along, at the same time, their performances have been improved tremendously. These innovations have to be attributed to the intensive progresses made on both theoretical and experimental studies in solid state physics. Furthermore, due to the advent of the economical high speed computers, the theoretical studies on crystalline materials have made the research even more progressive.

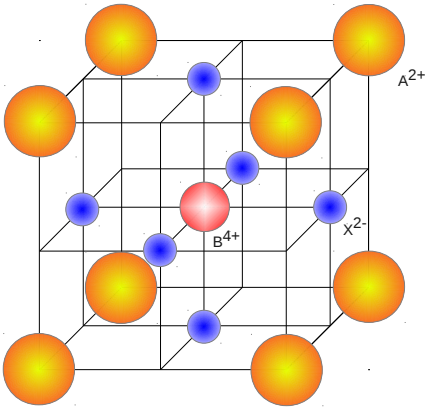

FIGURE 2.1: Conventional unit cell of a perovskite crystal.

2.1 Perovskite Structure

Perovskites are important in material science due to their interesting properties and useful applications in many areas.The physical properties of interest among perovskites include superconductivity, ferroelectricity, magnetic properties, electric conductivity, dielectric properties, etc. A lot of materials with perovskite structure have been discovered. Some of the compounds that possess perovskite structure are $CaTiO_3$, $BaTiO_3$, $SrTiO_3$, $CdTiO_3$, $PbTiO_3$, $SrZrO_3$, $BaZrO_3$, $KNbO_3$, $LiNbO_3$, $LiTaO_3$, $BaPrO_3$, $CsCaF_3$, $LiBaF_3$, and many more.

Perovskite structure, which has a very high symmetry, is a crystal structure with simple cubic lattice, as shown in Figure 2.1. The general chemical formula for perovskite compounds are ABX_3, where A and B are cations and X is an anion. A^{2+} and B^{4+} cations have different sizes, in which A^{2+} is larger than B^{4+}. A^{2+} ions are located at the corners of the cube, B^{4+} ions are located at the centers, and X^{2-} ions are located at the faces of the cube. Thus, there are five atoms in a conventional cell, and hence, five atoms per lattice point or five atoms in a primitive cell. X^{2-} anions are bonded to both A^{2+} and B^{4+} cations. Each B^{4+} cation has six nearest neighbours, whereas each A^{2+} cation

has twelve. Thus, B^{4+} and X^{2-} ions form octahedrons, while A^{2+} and X^{2-} ions form cuboctahedrons in the perovskite. The requirement of relative ionic sizes for stability of the perovskite is rigorous, so a slight distortion might cause the structure to reduce to a lower symmetry, in which the coordination numbers will be reduced.

2.2 Thermal Properties

One of our main interests in this work is to study thermal properties of materials. Therefore, it is important to understand how the expressions of the thermal properties are obtained. Hence, the derivations of heat capacity and thermal conductivity are shown here.

2.2.1 Derivations of Heat Capacities of Solids

Heat capacity is a measurable physical quantity that characterizes the amount of heat required to change the temperature of a substance of 1 kg by 1 K. In this section, the derivation of the specific heat from classical treatment is discussed.

Consider a solid system of N atoms held in their respective positions and are free to vibrate independently. In classical theory, the atoms are assumed to vibrate like classical harmonic oscillators. Thus, the atomic vibrations can be regarded as spring vibrations, which execute small vibrations about their equilibrium positions. The energies due to the motion of each atom along the three

directions are

$$E_x = \frac{p_x^2}{2m} + \frac{1}{2}kx^2 \tag{2.1}$$

$$E_y = \frac{p_y^2}{2m} + \frac{1}{2}ky^2 \tag{2.2}$$

$$E_z = \frac{p_z^2}{2m} + \frac{1}{2}kz^2 \tag{2.3}$$

where the spring constants k are taken to be the same along the three directions. If the temperature is sufficiently high, the atomic oscillators can be treated using classical statistical mechanics. At this point, it is useful to state the equipartition theorem (further discussion can be found in Section 3.4.3):

Equipartition Theorem

> For a system in thermal equilibrium at temperature T, a generalized position or momentum that occurs in the Hamiltonian only as a quadratic term contributes an energy of $\frac{1}{2}k_BT$ to the mean energy of the system, where k_B is the Boltzmann constant.

Thus, according to equipartition theorem, the mean energy of the solid of N atoms is

$$\begin{aligned} \bar{E} &= N(E_x + E_y + E_z) \\ &= 3N(\frac{1}{2}k_BT + \frac{1}{2}k_BT) \\ &= 3Nk_BT = 3RT \end{aligned} \tag{2.4}$$

where $R = 8.314$ J/Kmol is the gas constant. The specific heat of the solid is

$$\begin{aligned} C_V &= \left(\frac{\partial E}{\partial T}\right)_V \\ &= 3R = 24.94 \text{ J/Kmol} \end{aligned} \tag{2.5}$$

Some solids such as aluminium, copper and germanium, have specific heat values close to 24.94 J/Kmol. However, some substances such as diamond and silicon has a much lower specific heat value. This can be understood that the classical treatment is valid only when the temperature T is high enough so that $k_B T \gg \hbar\omega$, where $\hbar$ is the Planck constant and ω is the vibrational frequency. $C_V = 24.94$ J/Kmol is called the Dulong-Petit limit. Furthermore, note that Equation 2.5 does not depend on temperature. This is also incorrect as when the temperature goes to zero, the specific heat approaches zero as well. Thus, it can be concluded that the classical treatment only works fine at very high temperature. In order to obtain agreement at all temperatures, quantum mechanical treatment is required.

2.2.2 Derivation of Thermal Conductivity

If thermal conduction is viewed from a microscopic angle, the heat energy is transferred by the diffusion and collisions of particles, such as electrons, atoms, molecules and phonons within a body due to a temperature gradient. From a macroscopic point of view, a temperature gradient causes heat to flow from a region with higher temperature to a region with lower temperature. The heat flux, which is the heat energy crossing per unit area per unit time is expressed according to the Fourier's law of heat conduction:

$$J_x = -\kappa \frac{dT}{dx} \tag{2.6}$$

where dT/dx is the temperature gradient along the x direction and the coefficient κ is known as the thermal conductivity.

Imagine a slab in which the temperatures are varied. If only the x direction is considered, 1/6 of the particles will move toward the $+x$ direction, and similarly 1/6 of the particles will diffuse toward the $-x$ direction. Assume that the particles collisions happened at the middle of the slab along the x direction. If the mean free path of the particle collisions is let to be l, the last collisions of the particles which diffuse toward the $+x$ direction happen to be at position of $x - l$, whereas the last collisions of the counterparts take place at $x + l$. Therefore, the energies of the particles can be evaluated at these positions. Hence, the mean energy transported per unit area per unit time towards the $+x$ direction is

$$J_{+x} = \frac{1}{6} n\bar{v}\bar{E}(x - l) \tag{2.7}$$

and similarly, the mean energy transported per unit area per unit time towards the $-x$ direction is

$$J_{-x} = \frac{1}{6} n\bar{v}\bar{E}(x + l) \tag{2.8}$$

where n is the concentration of the particles, $\bar{v}$ is the mean velocity of the particles, and $\bar{E}(x + l)$ and $\bar{E}(x - l)$ are the mean energies of the particles at $x + l$ and $x - l$ respectively. Thus, the net energy flows per unit area per unit time or the net energy flux is

$$\begin{aligned} J_{net} &= J_{+x} - J_{-x} \\ &= \frac{1}{6} n\bar{v}[\bar{E}(x - l) - \bar{E}(x + l)] \\ &= \frac{1}{6} n\bar{v} \left\{ \left[\bar{E}(x) - l\frac{\partial \bar{E}}{\partial x}] - [\bar{E}(x) + l\frac{\partial \bar{E}}{\partial x} \right] \right\} \\ &= -\frac{1}{3} n\bar{v} l \frac{\partial \bar{E}}{\partial x} \end{aligned} \tag{2.9}$$

In terms of derivative of T, Equation 2.9 becomes

$$J_{net} = -\frac{1}{3} n\bar{v}l \frac{\partial \bar{E}}{\partial T} \frac{\partial T}{\partial x} \tag{2.10}$$

Since the heat capacity per unit volume of the particles is

$$C_V = n\frac{\partial \bar{E}}{\partial T} \tag{2.11}$$

Equation 2.10 becomes

$$J_{net} = -\frac{1}{3} C_V \bar{v}l \frac{\partial T}{\partial x} \tag{2.12}$$

Comparing between Equation 2.6 and Equation 2.12 yields

$$\kappa = \frac{1}{3} C_V \bar{v}l \tag{2.13}$$

Equation 2.13 has been used to calculate the thermal conductivity by phonons, where C_V is treated as the specific heat of phonons, $\bar{v}$ is taken to be the speed of sound and l is the phonon mean free path. Note that at high temperatures, where the temperatures are much higher than the Debye temperature ($T \gg \Theta_D$), C_V obeys the Dulong-Petit law and is temperature-independent. Therefore, the thermal conductivity should be expected to decline with increasing temperature in the high-temperature regime, and the rate of decline is generally given by

$$\kappa \propto \frac{1}{T^{\eta}} \tag{2.14}$$

where η is somewhere between 1 and 2.

Chapter 3

Background Theory II - Molecular Dynamics

Molecular dynamics (MD) simulation is one of the powerful computer simulation techniques in the sense that it not only allows prediction of material's properties at macroscopic level, it also helps to understand the basic physics behind the macroscopic bahavior.

In MD simulation, we provide a 'guess' for the interatomic interactions and obtain 'exact' predictions of bulk properties. The predictions are exact in the sense that they can be made as accurate as we like, subject to the limitation of computer budget.

Besides, MD simulations also act as a bridge between theory and experiment, i.e. a theory may be tested by performing simulation using the same model, on the other hand, simulations may be carried out on the computers which are difficult or impossible to be performed in the laboratories, for example, working at extremes of temperature and pressure. Ultimately, we would like to make direct

comparisons with the experimental measurements made on specific materials, in which a good model of molecular interactions is essential.

The basic idea of MD simulation is to simulate the motions and assemblies of the atoms and molecules[1]. In other words, MD simulation provides means to solve the equation of motions of the interacting particles. Once the information of the system at the atomic level is known, macroscopic physical quantities are revealed via statistical mechanics.

3.1 Equations of Motion

Consider a system of N interacting particles, such as atoms and molecules, the Lagrange equations of motion are:

$$\frac{dL}{dx_k} - \frac{d}{dt}\left(\frac{dL}{d\dot{x}_k}\right) = 0 \tag{3.1}$$

where $k = 1, 2, 3$, and x_i and $\dot{x}_i$ are the generalized coordinates and velocities respectively. L is the Lagrangian of the particle:

$$L(x, \dot{x}) = K(\dot{x}) - U(x) \tag{3.2}$$

where K and U are the kinetic and potential energies of the particle.

If a system of atoms in Cartesian coordinates r is considered, the quantitative account of the Newton's second law of motion gives:

$$F_i = m_i \ddot{r}_i \tag{3.3}$$

[1] We shall called them particles for simplicity.

where m_i is the mass of the i^{th} particle, and

$$F_i = -\nabla U(r_i) \tag{3.4}$$

is the force experienced by the i^{th} particle.[2] Thus, solving Equation 3.3, which required the knowledge of the potential energy (Equation 3.4), gives the positions and velocities of the particles.

3.2 Non-bonded Molecular Interactions

In order to solve the equations of motion, a preliminary step is to determine the potential energy of the atomic system. The molecular interactions can be decomposed into non-bonded interactions and bonding interactions. In this section, non-bonded interactions are focused and the discussion on molecular bonding can be found elsewhere [34]. The non-bonded potential energy of the system of N interacting particles is formulated as a sum over the interactions between the particles in the system:

$$U(r) = \sum_i u(r_i) + \sum_i \sum_{j>i} v(r_i, r_j) + \sum_i \sum_{j>i} \sum_{k>j>i} w(r_i, r_j, r_k) + \dots \tag{3.5}$$

where the summations sum over all distinct pairs without counting any pair twice. The first term $u(r_i)$ characterizes an externally applied potential field or the effect of the container walls. However, when periodic boundaries are concerned, this term is usually ignored. The second term $v(r_i, r_j)$ represents a two-body potential and the third term $w(r_i, r_j, r_k)$ typifies a three-body potential. In most cases, the potential energy of the system is usually simplified into two-body potential or

[2] These equations also apply to molecules, where F_i is the total force experienced by i^{th} molecule at its center of mass.

pairwise potential, $v(r_i, r_j) = v(r_{ij})$, where r_{ij} is the distance between the i^{th} and j^{th} particles. Some of the most commonly used pairwise potential functions[3] will be discussed.

3.2.1 Lennard-Jones Potential

Lennard-Jones potential, which is also known as $6-12$ potential, is one of the earliest and most commonly used potentials. It is associated with Van der Waals (weak) interaction or dipole $-$ dipole dispersion. The functional form is

$$U_{LJ}(r_{ij}) = 4\phi[(\frac{\chi}{r_{ij}})^{12} - (\frac{\chi}{r_{ij}})^{6}] \tag{3.6}$$

where ϕ and χ are constant parameters that set the energy and distance scales associated with the interactions. The first term or the term to the power of 12 contributes repulsive force and the second term or the term to the power of 6 contributes attractive force. This potential has been used in the early studies of liquid Argon. For Argon, the optimised parameters are $\phi/k_B = 119.8$ and $\chi = 3.405$Å.

3.2.2 Born-Mayer-Huggins Potential

Another type of potential which also describes Van der Waals interaction is the Born-Mayer-Huggins potential or exponential $-$ 6 potential:

$$U_{Born}(r_{ij}) = f_0(\rho_{ij}) \exp\left(\frac{\sigma_{ij} - r_{ij}}{\rho_{ij}}\right) - \frac{C_{ij}}{r_{ij}^6} + \frac{\zeta_{ij}}{r_{ij}^8} \tag{3.7}$$

[3]For connections among the pairwise potential functions, see [35, 36].

where σ_{ij} represents the sum of ionic radii of i^{th} and j^{th} ions, ρ_{ij} symbolies the sum of ionic softness of i^{th} and j^{th} ions, and C_{ij} and ζ_{ij} correspond to dipole − dipole dispersion and dipole − quadrupole dispersion parameters respectively. The first term represents the exponential repulsion at short-range, the second term corresponds to Van der Waals attraction and the third term represents dipole − quadrupole dispersion.

3.2.3 Coulombic Potential

If electrostatic charges are presents in the system, there will be ionic or Coulombic forces interacting the ions in such a way that like charges repel each other, whereas opposite charges attract. The magnitudes of the forces depend on the electrostatic charges, thus, we have Coulombic potential:

$$U_{Coulomb}(r_{ij}) = k_e \frac{q_i q_j}{r_{ij}} \tag{3.8}$$

where q_i and q_j are the electrostatic charges of i^{th} and j^{th} ions, and k_e is the Coulomb constant.

3.2.4 Morse Potential

When dealing with 'hard' bonds, such as covalent bonds, it is useful to employ Morse potential. Morse potential is an empircal potential that describe an asymmetric covalent bonding between two ions, and it also accounts for bond breaking. The functional form of Morse potential is

$$U_{Morse}(r_{ij}) = D_{ij}\{\exp[-2\Omega_{ij}(r_{ij} - r_{0ij})] - 2\exp[-\Omega_{ij}(r_{ij} - r_{0ij})]\} \tag{3.9}$$

where D_{ij} is the depth of the potential well, Ω_{ij} is the steepness of the potential and r_{0ij} is the equilibrium distance between the ions. Unlike harmonic bonding, Morse potential caters the anharmonicity of real bond, which is more harder to compress than pull it apart, and this anharmonicity also contributes to material's thermal expansion.

3.3 Molecular Dynamics Algorithms

The basic idea in MD simulation is to solve the equations of motion, i.e. Equation 3.3. For each particle, the equations of motion according to Euler method are

$$\frac{dr_i}{dt} = v_i \tag{3.10}$$

and

$$\frac{dv_i}{dt} = \frac{F_i}{m_i} = a_i \tag{3.11}$$

where v_i and a_i are the resultant velocity and acceleration of i_{th} particle. If we choose a value δt to be the size of every time step, the one step of the equations of motion are

$$r_i(t + \delta t) = r_i(t) + v_i(t + \delta t/2)\delta t \tag{3.12}$$

and

$$v_i(t + \delta t) = v_i(t) + a_i(t + \delta t/2)\delta t \tag{3.13}$$

With the knowledge of the potential energies of the particles, the forces or accelerations can be derived, and thus, the atomic positions and velocities can be obtained. However, in MD simulation, we are interested in computing the motion over a very large number of time steps, and it turns out that the numerical

errors associated with Euler method are too big to tolerate. When accuracy is concerned, it is necessary to employ other scheme for solving the equations of motion.

3.3.1 Verlet Algorithm

Verlet algorithm [37] has smaller numerical errors associated if compared with Euler method. In order to derived the Verlet algorithm, we take Taylor expansion about $r_i(t)$, which yields:

$$r_i(t+\delta t) = r_i(t) + \delta t\ v_i(t) + (1/2)\delta t^2 a_i(t) + \dots \tag{3.14}$$

$$r_i(t-\delta t) = r_i(t) - \delta t\ v_i(t) + (1/2)\delta t^2 a_i(t) - \dots \tag{3.15}$$

Summing up Equations 3.14 and 3.15 gives

$$r_i(t+\delta t) = 2r_i(t) - r_i(t-\delta t) + \delta t^2 a_i(t) \tag{3.16}$$

Equation 3.16 is the ordinary Verlet algorithm for trajectories. It is remarkable to note that knowing the advanced positions only required the positions at both present and previous step, and also the accelerations at present step. Furthermore, it does not require the knowledge of the velocities. Although velocities are not needed to compute the trajectories, they are useful for estimating the kinetic energy (and hence the total energy). Taking the difference between Equations 3.14 and 3.15 produces the formula for velocities

$$v_i(t) = \frac{r_i(t+\delta t) - r_i(t-\delta t)}{2\delta t} \tag{3.17}$$

Note that the errors per integration step associated with Verlet algorithm are of the order of δt^4 for Equation 3.16 and δt^2 for Equation 3.17.

3.3.2 Timesteps

It is important to choose a proper time step δt in MD simulation. The time step should be large enough so that the time averages can be close to the averages in a macroscopic experimental system, and conversely, it should be small enough so that the computational resource is enough to ensure that time averages can be evaluated over a sufficient number of times. A typical time step used to integrate the equations of motion numerically is about 10^{-15} s or 1 fs. Since $\sim 10^6$ integration steps are normally adopted for a reasonable computing time, the simulation is restricted to about 10^{-9} s or 1 ns.

3.3.3 Periodic Boundary Condition

In a real system, where the number of particles is significantly large ($\sim 10^{23}$), the collisions between the particles and the walls of the container are negligible, since the system behavior would be dominated by collisions between particles. However, in computer simulation, the number of particles is not significantly large due to the limitation of computational resouces. In other words, we are limited to a small system, which contains a relatively small number of particles ($\sim 10^3$). Hence, the collisions between the particles and the walls can be significant and non-negligible. For example, consider 1000 atoms arranged in a $10 \times 10 \times 10$ cube, nearly half the atoms are on the outer faces, and the collisions between these particles and the walls will have a large effect on the measured properties. Therefore, it is useful to implement a periodic boundary condition.

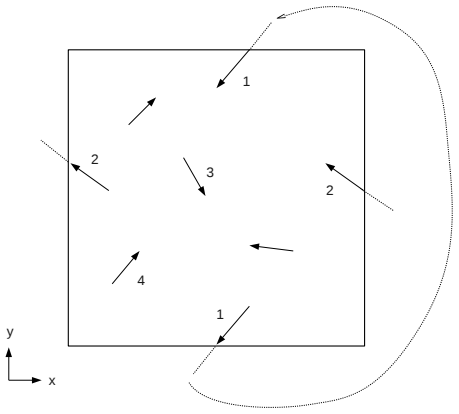

FIGURE 3.1: Schematic diagram of periodic boundary condition.

To understand periodic boundary condition, imagine that a particle is approaching a wall, and when the particle hits the wall, it is instantaneously transported to the opposite side of the wall and is like coming from that wall, as shown in Figure 3.1. By doing this, the collisions between the particles and the walls will be absolutely zero. It is important to bear in mind that even though the particle is transported to the opposite side, it can still affect the particle near the wall side because the particle can also be imagined to locate beyond the boundary. Thus, in order to calculate the particle interactions with periodic boundary condition imposed, the minimum image convention is adopted, in which the particles interact with the nearest particle or image in the periodic array. Therefore, this solve the boundary problem. However, special attention must be paid when considering properties which are influenced by long-range correlations, such as the imposed artificial heat flow in NEMD method.

3.3.4 Cut-off radius

In order to compute the particles' trajectories using Verlet algorithm, i.e. Equation 3.16, we have to, first of all, calculate the interatomic forces, which can be

obtained by computing the potential energies according to Equation 3.4. However, computing the non-bonded interatomic forces involved a great number of pairwise calculations if the potential energy has an infinite range, i.e. when considering each particle i, the force calculations are loop over all other particles j in order to obtain the atomic seperation r_{ij}. Since the potential energy becomes zero when the atomic seperation r_{ij} is very large, it is useful to implement a cut-off radius r_c and truncate the interatomic interactions when the interatomic seperation is greater than r_c. In other words, the force calculations are skipped if $r_{ij} > r_c$ and move on to consider other j particle. By this way, expensive calculations can be avoided and enormous computational resouces can be saved[4]. A typical cut-off radius r_c has a value of about 12 Å.

If cut-off radius is implemented, there will be a truncation in interatomic interactions. For example, when a particle crosses the cut-off radius, there will be a little 'jump' in the energy, and this creates a new problem as it will destroy the conservation of the energy. In order to correct for the energy, a tail correction is usually implemented. See [38] for more details.

3.3.5 Neighbour Lists

Although the force calculations can be skipped when the atomic seperation is greater than the cut-off radius, when examining the condition of $r_{ij} > r_c$ for all other particles j, this still consumes plenty of time. Verlet [37] suggested

[4]In order to understand this better, imagine that you have a mess of marbles on the floor but dispersed uniformly and you draw two circles with the their center overlapped and the radius of the second circle r_2 greater than that of the first one r_1, for instance $r_1 = 5$cm and $r_2 = 10$cm. If you count the number of marbles in the circles, you will find that the number of marbles in the circle with larger radius is not twice but is multiple times (about 4 times) of the number of marbles in the smaller circle, even though the radius of the second radius is twice as big as that of the fircle circle. In other words, calculation twice as big takes four times as long to complete. Thus, by skipping the calculations over the particles which are confined in the larger radius, great computing time can be saved.

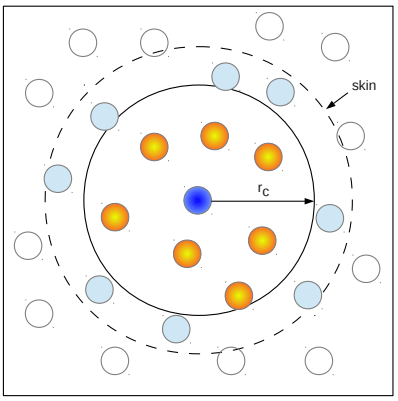

FIGURE 3.2: Schematic diagram of neighbour lists. Only pairs appearing in the list are checked in the force routine.

that construction of lists of nearby pairs of particles can be used to improve the speed of the program. To construct the so-called neighbour lists, each particle is surrounded by a 'skin', which has a radius slightly larger than the cut-off radius, and only particles that fall within the skin are listed as 'neighbours', as shown in Figure 3.2. Hence, each particle has a unique neighbour list. When the force calculations are carried out, only particles within the list are checked, and thus, this save a large amount of computing time, even though the lists need to be reconstructed from time to time. The choice of the skin radius, which is the distance between the skin and the cut-off radius, is a compromise, i.e. larger lists require less frequent update, but consume more computer time compared with smaller lists. So, the choice of skin radius need to be made by experimentation. A typical skin radius is about 2 Å.

3.4 Statistical Mechanics

In molecular dynamics simulation, we are not dealing with one or two particles, but we are dealing with a bunch of them. So, in order to understand the macroscopic behavior of a system with numerous particles, probabilities and statistics of the microscopic system have to be used to predict the macroscopic properties, which can be measured in the laboratory (like temperature, pressure, etc.). That's why statistical mechanics is important as it act as a bridge between atomic simulation and macroscopic properties, in which the properties of macroscopic bodies are predicted by the statistical behavior of their constituent microscopic parts. Therefore, with molecular dynamics simulation, which generate information at microscopic level, thermodynamic properties of the atomic system can be studied via statistical mechanics.

3.4.1 Ensembles

An ensemble is a collection of all possible systems which have an identical thermodynamic state but have different microscopic states.

In classical molecular dynamics, simulations are easily done in the microcanonical ensemble (NVE-constant), in which the number of particles, volume and energy are controlled. However, in real life, the temperature and/or pressure are controlled instead of the energy. In other words, the real-life physical properties are observed in canonical ensemble (NVT-constant) or isothermal-isobaric ensemble (NPT-constant). Thus, it is more useful to carry out the simulation in canonical ensemble or isothermal-isobaric ensemble, so that the simulated results are comparable to the experimental properties. Several popular methods that used to control the temperature in MD simulation are the velocity rescaling

method, Andersen thermostat, Nose-Hoover thermostat [39], Langevin thermostat [40], etc.

3.4.2 Time Average

In MD simulation, various physical quantities are monitored and their expectation values are determined by taking averages over the total configurations generated in the simulation or over the total time steps τ. Such averages are denoted as 'time average', although the word time does not necessarily mean physical time. For a physical quantity Q, the time average is

$$\bar{Q} = \frac{1}{\tau}\sum_{n=1}^{\tau} Q_n \tag{3.18}$$

If the size of the system is large enough and the simulation is long enough, these averages will be very close to the averages in a macroscopic experimental system, i.e. the ensemble averages, as according to the Ergodic hypothesis. Ensemble average is an average taken over many replicas of the system considered simultaneously. However, the system size and simulation time that can be achieved are limited, and hence, it might be useful to estimate the errors associated with the averaged quantities. The standard deviation ς associated with Equation 3.18 is

$$\varsigma = \sqrt{\bar{Q}^2 - \bar{Q}^2} \tag{3.19}$$

Note that equation 3.19 is a crude way to estimate the errors associated with the measured averaged quantities, because the data points generated from the simulation are usually not independent, conversely they are highly correlated since the configurations are usually stored sufficiently and frequently. Therefore,

a correlation time should be added in order to estimatate the errors with higher precision.

3.4.3 Equipartition Theorem

One of the important quantities for a system in thermal equilibrium is the temperature. In MD simulation, the temperature T does not enter as an input parameter, it has to be measured instead. In order to measure the temperature of a molecular system, we make use of equipartition theorm.

Equipartition theorm states that *for a classical system an energy of* $\frac{1}{2}k_BT$ *is associated with any degree of freedom that enters the energy quadratically*, where k_B is the Boltzmann constant. Since the kinetic energy K of a particle with mass m is

$$K = \frac{1}{2}m(v_x^2 + v_y^2 + v_z^2) \tag{3.20}$$

where v_x, v_y, v_z are the x, y, z components of the particle's velocity, so the equipartition theorem states that for a system in thermal equilibrium,

$$\frac{3}{2}k_BT = \langle\frac{1}{2}m(v_x^2 + v_y^2 + v_z^2)\rangle \tag{3.21}$$

where the angular bracket $\langle \dots \rangle$ denotes a double averages, i.e. time average of the kinetic energy per particle averaged over all of the particles. Thus, by measuring the velocities of the particles using Equation 3.17, the temperature of the system can be measured using Equation 3.21.

Chapter 4

Methodology

In this chapter, I shall explain all the steps and methods that have been used in this study. They are explained in detail so that the results can be reproduced.

4.1 Potential Model

Since the basic idea of molecular dynamics simulation is to simulate the motions and assemblies of the atoms based on the atomic interactions, the preliminary step is to obtain a reliable interatomic potential interactions of the system. Deriving an accurate and reliable potential is important because the quality of the interatomic potential is the key factor to the correctness of the prediction of macroscopic properties.

A few general beliefs about potential are pointed out. First, the potential developed here is a classical potential, and most classical potentials are not transferable, i.e. these potentials can only be used when close to the state where they were parameterized for. For example, the potential parameters derived in this

study should work fine in the temperature range from room temperature up to a high temperature of 2000 K, and in the pressure range from 1 atm to 20.3 GPa. Second, if the potential is modeled to study for certain phenomena, the results might deviate if it is used to study for other properties; the farther away from the condition where a set of potential is derived for, the less accurate the results will be. For example, our goal of parameterization is that eventually we would like to obtain accurate results of various thermodynamic properties. Therefore, the potential developed here is not advisable to be adopted to study for other properties or phenomena, such as phase transition.

In this study, a simple pairwise potential has been used to represent the intricate interatomic interactions. The pairwise potential, which consists of Coulombic (ionic) interaction, short-range repulsion, Van der Waals attraction and Morse-type covalent bonding, is reliable to model multi-component oxides [41] and is shown below:

$$\begin{aligned} U(r_{ij}) &= \frac{q_i q_j}{r_{ij}} + f_0(\rho_{ij}) \exp\left(\frac{\sigma_{ij} - r_{ij}}{\rho_{ij}}\right) - \frac{C_{ij}}{r_{ij}^6} \\ &\quad + D_{ij}\{\exp[-2\Omega_{ij}(r_{ij} - r_{0ij})] - 2\exp[-\Omega_{ij}(r_{ij} - r_{0ij})]\} \end{aligned} \tag{4.1}$$

where i and j refer to the type of ions in a unit cell: $i, j \in \{\mathrm{Sr}, \mathrm{Ba}, \mathrm{Ti}, \mathrm{Zr}, \mathrm{O}\}$. The first term typifies Coulombic potential, where q_i and q_j are the effective charges of the i^{th} and j^{th} ions and r_{ij} is the distance between them. The second term represents short-range repulsion, where $\sigma_{ij} = \sigma_i + \sigma_j$, $\rho_{ij} = \rho_i + \rho_j$, and σ_i and ρ_i embody ionic radii and ionic softness respectively. $f_0 = 1.0$ kcal $\mathrm{\AA}^{-1}$ mol^{-1} is the force constant. The third term characterizes Van der Waals attraction, where $C_{ij} = C_i C_j$ and C_i is the Van der Waals attraction parameter. The last term represents Morse-type asymmetric stretching and compression of the interatomic

covalent bonding, where D_{ij} is the depth of the potential well, Ω_{ij} is the potential steepness and r_{0ij} is the equilibrium distance between the ions.

4.2 Potential Parameterization

Getting the right values of the parameters in Equation 4.1 is the most arduous step among all, yet the most crucial one. In this section, I shall explain how the potential is parameterized for strontium titanate and barium zirconate. I shall begin with strontium titanate first.

For $SrTiO_3$, to our knowledge, there are two sets of potential parameters found in the literature, i.e. published by Katsumata *et al* [42] and Seetawan *et al* [1]. Since, they have already derived and implemented potentials for the material, all we need to do is to check whether the potential is reliable and transferable into our study.

First, when we were trying to reproduce the results using the potential parameters of Seetawan *et al* [1], a fatal error has been found in their potential: their set of potential parameters has an unphysical attraction between Sr and O at close range, i.e. their attractions get stronger when they get closer to each other instead of repulsing each other, which causes the simulation to be unstable and leads to failure of reproducing the lattice parameters at high temperatures. The fact that Katsumata *et al* 's [42] lattice parameters are able to be reproduced using their potential parameters even to high temperatures strengthen the case that Seetawan *et al* reproduction at high temperatures has been overlooked and is wrongly presented. The unphysical attraction of $Sr - O$, which introduced by Seetawan *et al* is discussed in detail in Section 5.1.2.

Second, according to Katsumata *et al* [42], their potential parameters are not fully optimized to simulate other physical properties, other than lattice parameter, thermal expansion and compressibility. Most probably is that their potential is parameterized only for certain properties. This also implies that their potential parameters need to be improved in order to calculate other properties, such as heat capacity and thermal conductivity.

Due to these two reasons, we are motivated to parameterize some of the potential parameters. q_i, σ_i, ρ_i, $D_{\mathrm{Ti-O}}$, $\Omega_{\mathrm{Ti-O}}$ and $r_{0\mathrm{Ti-O}}$ parameter values of Katsumata *et al* [42] have been adopted, but their Van der Waals parameters C_i have been ignored. The Van der Waals attractive parameters were parameterized based on an assumption that the Van der Waals attraction is only significant between anion - anion pairs. Hence, C_{Sr} and C_{Ti} are assumed to be zero and C_{O} is determined by fitting the simulation results against the experimental lattice parameters.

On the other hand, for $BaZrO_3$, to our knowledge, there exist one set of potential parameters, which is published by Kurosaki *et al* [43]. However, their potential is not accurate enough to account for some important properties. For instance, the value of thermal conductivity at room temperature obtained by them is about 8.71 m^{-1} K^{-1}, and this value has a deviation of about 102 % compared to experimental value of Vassen *et al* [10] of about 4.31 m^{-1} K^{-1}. Therefore, we would like to derive a more accurate potential parameters for $BaZrO_3$.

Trial and error is the strategy: all values were determined by trial and error, except for the parameters of O^{2-} ion, i.e. σ_O, ρ_O and C_O, which are taken from the potential of $SrTiO_3$ of Katsumata *et al* [42]. The trial-and-error protocol is summarized as follows:

1. An initial guess of the potential parameters was made.

2. The conjectural parameters were fed into the simulations to calculate the lattice parameters at three conditions: (i) room temperature and ambient pressure, (ii) higher temperature and ambient pressure, and (iii) room temperature and higher pressure.

3. The calculated lattice parameters were checked for the agreement with the experimental lattice parameters. If they are mismatched, the potential parameters will be changed randomly, and proceed to step 2.

4. Steps 2 and 3 were repeated until the calculated lattice parameters match with the experimental values.

The aforementioned protocol has been programmed in shell scripts to expedite the calculations. Essentially, the potential parameters were determined by fitting the numerical results against the variations of experimental lattice parameters with temperature and pressure.

TABLE 4.1: Potential parameters of $SrTiO_3$ and $BaZrO_3$. The last two rows show the parameters of the Morse-type potential.

Ion	q_i(e)	σ_i(Å)	ρ_i(Å)	C_i(kcal$^{\frac{1}{2}}$ Å^3 mol$^{-\frac{1}{2}}$)
Sr	2.00[a]	1.8460[a]	0.1300[a]	0
Ba	2.00	2.0199	0.1573	0
Ti	2.20[a]	1.3850[a]	0.1000[a]	0
Zr	2.20	1.4901	0.08617	0
O	−1.40[a]	1.8500[a]	0.1800[a]	25.04
Ions	D_{ij}(kcal mol^{-1})	Ω_{ij}(Å^{-1})	r_{0ij}(Å)	
Ti − O	26.00[a]	2.000[a]	1.600[a]	
Zr − O	24.38	2.047	1.785	

[a] Obtained from [42].

In summary, the potential parameters of $SrTiO_3$ and $BaZrO_3$ used in this study are shown in Table 4.1. Notice that the potential parameters of O ion is

transferable between $SrTiO_3$ and $BaZrO_3$ perovskite materials. It can be seen from the table that the parameters of the Morse-type potential assume non-zero values only for $Ti - O$ and $Zr - O$ pairs. Also, notice that the Coulombic charges of the ions are not adhering to full ionic charge, but with partial ionic charge; these effective partial ionic charges are granted to mimic the average electric charge distributions.

4.3 Simulation Protocol

Once the potentials (force field [1]) of the systems have been determined, the molecular dynamics simulation can be set up. The protocol of the simulation is described below:

- The simulation first started at 298 K and 1 atm, as the simulation is believed to work well above these conditions due to the classical basis of the program.
- In each unit cell, the A-type cations were located at (0, 0, 0), B-type cations were located at (0.5, 0.5, 0.5) and X-type anions were located at (0.5, 0.5, 0), (0.5, 0, 0.5) and (0, 0.5, 0.5). A=(Sr,Ba) ; B=(Ti,Zr) ; X=(O).
- Simulation cells of size correspond to $8 \times 8 \times 8$ unit cell, which consists of 2560 atoms were created.
- Particles' velocity were generated according to the Maxwell-Boltzmann velocity distribution.

[1] In the context of molecular modeling, a force field refers to a mathematical form with parameters to describe the potential energy of a system of particles (atoms, molecules etc.), like Equation 4.1. In physics, the term force field is usually direct to a vector force experienced by a particle when it is in a vector field, such as gravitational field or electric field. Therefore, I prefer to use the word potential rather than force field to avoid misunderstanding.

- In order to solve the equation of motion, Verlet algorithm (Equation 3.16) with a time step δt of 1.0 fs was used.
- Simulation in canonical ensemble and isothermal-isobaric ensemble were performed using Nose-Hoover algorithm [39] with a time constant of 0.1 ps for thermostat and 1.0 ps for barostat.
- A global cut-off distance r_c of 11.0 Å was adopted.
- Long-range Van der Waals tail correction [38] was added.
- Ewald summation [44] with a precision of 10^{-4} was used for the long-range Coulombic interaction.
- Periodic boundary condition was imposed.
- Initially, all systems were equilibrated for 20,000 time steps.
- After that, the macroscopic properties were obtained by time averaging of 100,000 time steps.

Note that the choices of the parameters used are determined by performing convergence tests. At this point, a program can be written to perform the molecular dynamics simulation. Since some powerful molecular dynamics codes, such as LAMMPS [45] and MXDTRICL [46], are freely available, we can just used them to perform the simulations. In this study, the simulations were carried out using open-source LAMMPS [45], which stands for Large-scale Atomic/Molecular Massively Parallel Simulator. The input scripts of LAMMPS are shown in Appendix A.

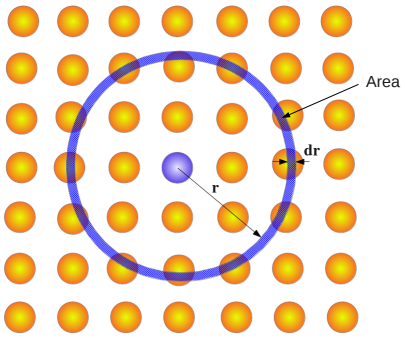

FIGURE 4.1: Schematic diagram of radial distribution function.

4.4 Extraction of Physical Quantities

In this section, I shall explain how the results were obtained from the simulation. I shall start with microscopic property, i.e. the radial distribution function first, and then follow by macroscopic thermodynamic properties.

4.4.1 Radial Distribution Function

In order to study the correlation between particles (atoms, molecules etc.) in the system, radial distribution function is derived from the simulation by binning the interatomic distances from a reference particle into 10,000 bins from 0 to the global cut-off distance of 11.0 Å. The sizes of the bins are uniform in radial distance. Thus, each bin can be imagined as a thin shell in three dimensional space, and a thin ring in two dimensional space. The basic idea is depicted in Figure 4.1. The area of the thin ring is known as bin. Particles[2] which fall within the area of the ring were counted for each bin.

[2]Each particle is treated as a point particle, so do not worry about particles partially fall within a bin, it is either the whole particle fall within a bin, or it does not.

4.4.2 Temperature, Pressure and Energies

The temperature T of the system is measured using Equation 3.21, i.e. according to Equipartition theorem, whereas the pressure P is measured in term of virial expression:

$$P = \frac{Nk_BT}{V} + \frac{\langle \sum_i^N r_i \cdot f_i \rangle}{3V} \tag{4.2}$$

where N is the number of particles in the system, k_B is the Boltzmann constant, V is the volume and f_i is the force experienced by particle i at position r_i. The second term is virial. For pairwise potential, Equation 4.2 becomes

$$P = \frac{Nk_BT}{V} + \frac{1}{3V}\langle \sum_{i<j} r_{ij} \cdot f_{ij} \rangle \tag{4.3}$$

where r_{ij} and f_{ij} are the interatomic seperation and force between particles i and j.

The kinetic energy K of the system is computed by the formula

$$K = \sum_{i=1}^{N} \frac{1}{2} m_i (v_{x,i}^2 + v_{y,i}^2 + v_{z,i}^2) \tag{4.4}$$

where m_i and $v_{x,i}, v_{y,i}, v_{z,i}$ are the mass and x, y, z velocity components of particle i. The potential energy of the system is calculated using Equation 4.1 and Table 4.1. The total energy is obtained as the sum of kinetic energy and potential energy of the system.

4.4.3 Structural Parameters

Structural parameters such as lattice parameters, angles, molar volume, density, bond lengths etc. were obtained from the simulation in isothermal-isobaric

(NPT-constant) ensemble. In order to calculate, for example, molar volume of the system, simulation of 100,000 time steps was performed after the equilibration of the system, and volume of the simulation box was measured at each time step. The measured values were then averaged by total time steps according to Equation 3.18. The time-averaged volume was then compared with the experimental value. Although experimental observations are assumed to be esemble averages, according to Ergodic hypothesis, the time average is equal to the ensemble average. The calculations of the other structural parameters were basically similar as mentioned above.

4.4.4 Linear Thermal Expansion Coefficient

Linear thermal expansion coefficient, α can be calculated from the thermal variation of lattice parameter according to the following equation:

$$\alpha = \frac{1}{a_0}\left[\frac{da(T)}{dT}\right] \tag{4.5}$$

where a_0 is the lattice parameter at 298 K, and $da(T)/dT$ is the rate of change of the lattice parameter $a(T)$ in temperature T.

4.4.5 Isothermal Compressibility

Isothermal compressibility, β_T, which is a reciprocal of bulk modulus, is obtained from the variation of volume with pressure according to the following equation:

$$\beta_T = -\frac{1}{V_0}\left[\frac{dV(P)}{dP}\right] \tag{4.6}$$

where V_0 is the volume at 1 atm, and $dV(P)/dP$ is the rate of change of the volume $V(P)$ per unit change in pressure P.

4.4.6 Heat Capacity

Heat capacity at constant pressure, C_P is defined as:

$$C_P = \left(\frac{dH}{dT}\right)_P \tag{4.7}$$

where $H = E + PV$ is the enthalpy of the system, P is the external pressure, V is the volume and E is the system's internal energy. In order to evaluate this thermodynamic quantity, values of H were calculated via isothermal-isobaric (NPT-constant) simulation in the temperature range of 298 - 2000 K. C_P is then obtained from the variation of enthalpy H with temperature, according to Equation 4.7.

4.4.7 Thermal Conductivity

In molecular dynamics simulation, the two most common methods for studying thermal conductivity are the non-equilibrium molecular dynamics[3] (NEMD) method and the Green-Kubo method. In NEMD method, which is proposed by Müller-Plathe [47], thermal conductivity is calculated as the ratio of heat flux and temperature gradient, where the heat flux is imposed through kinetic energy exchange and the temperature gradient is the system's response. In Green-Kubo method, which involves equilibrium molecular dynamics, thermal conductivity is

[3]This method is known as non-equilibrium in the sense that the kinetic energy of the system is non-equilibrium, as it is highest at the middle of the rectangular bar and lowest at the two ends.

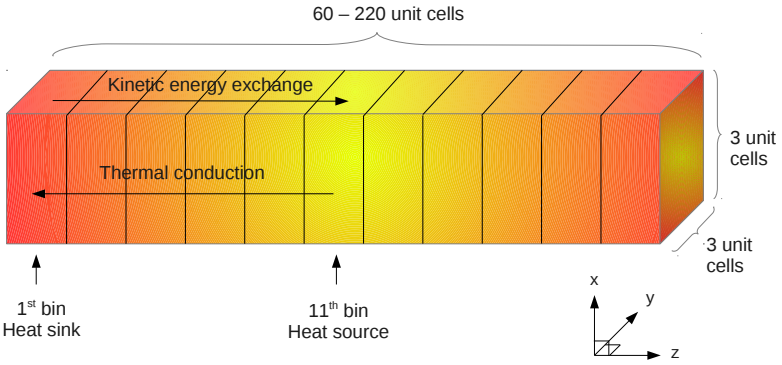

FIGURE 4.2: Schematic diagram of NEMD thermal conduction.

determined from the ensemble-averaged heat flux autocorrelation[4] function: it starts by calculating the instantaneous heat flux from the phase space configuration at time t, and the thermal conductivity tensor is then obtained by integrating the ensemble average of the time correlation function of the heat flux. In this study, thermal conductivity calculations of $SrTiO_3$ and $BaZrO_3$ were carried out using NEMD method in canonical ensemble (NVT-constant).

4.4.7.1 NEMD Method

A schematic diagram of non-equilibrium molecular dynamics method is depicted in Figure 4.2. Initially, each of the simulation cells of size varies from $3 \times 3 \times 60$ to $3 \times 3 \times 220$ unit cell, which looks like a rectangular bar, was divided into 20 bins along the z direction. After that, the highest particle's kinetic energy, K_{hot} from the 1^{st} bin was exchanged with the lowest particle's kinetic energy, K_{cold}

[4]Autocorrelation, which is also known as time correlation, is the cross-correlation of a signal with itself. In other words, it is a measure of how correlated a signal at a certain time to its value at another time.

from the 11^{th} bin continually at a specific frequency of 150 time step. Thus, a temperature gradient along the system or the bar can be induced, where the 11^{th} bin became the hottest slab and the 1^{st} bin became the coldest slab. The total energy transferred or heat flux, J_z along the z direction is given by:

$$J_z = \frac{\sum(K_{hot} - K_{cold})}{2tL_xL_y} \tag{4.8}$$

where the summation cumulates all the heat energy transferred through a surface area of $L_x \times L_y$ during the simulation run of time t. Note that the factor of 2 accounts for the fact that energy can flow from the heat source (11^{th} bin) to the heat sink (1^{st} bin) and also the other way round; the kinetic energy is artificially transferred from the cold slab to the hot slab, and then flows back from the hot slab to the cold slab through heat conduction. Finally, the temperature gradient along the z direction, dT/dz was measured, and the thermal conductivity, κ was calculated according to the Fourier's law:

$$\kappa = -\frac{J_z}{dT/dz} \tag{4.9}$$

4.4.7.2 Correction for Finite Size Effects

The scattering of phonon with the system's boundaries will limits the values of thermal conductivity. In non-equilibrium molecular dynamics (NEMD), this finite size effect is non-negligible, especially when the simulation length is not significantly larger than the phonon mean free path. A simple approach to correct for the finite size effects is to employ an extrapolation of thermal conductivity to an infinite-size system [48].

From the kinetic theory of gases, the thermal conductivity, κ can be expressed as:

$$\kappa = \frac{1}{3}\varrho c_V \nu l \tag{4.10}$$

where ϱ is the density, c_V is the constant-volume specific heat, ν is the speed of acoustic wave and l is the phonon mean free path. The phonon mean free path can be split into a bulk contribution, arising from the scattering among phonons, and a boundaries contribution, arising from the scattering of phonon with the boundaries, the heat source and the heat sink [48]:

$$\frac{1}{l_{MD}} = \frac{1}{l_{bulk}} + \frac{2}{L_z} \tag{4.11}$$

where L_z is the simulation length along the z direction, and the factor of 2 accounts for the fact that the phonon scattering occurs not only at the heat source and the heat sink, but at the boundaries as well. Substitution of Equation 4.11 into Equation 4.10 yields:

$$\frac{1}{\kappa_{MD}} = \frac{3}{\varrho c_V \nu}\left(\frac{1}{l_{bulk}} + \frac{2}{L_z}\right) = m\left(\frac{1}{L_z}\right) + \frac{1}{\kappa_{bulk}} \tag{4.12}$$

where $m = 6/(\varrho c_V \nu)$ and $\kappa_{bulk} = (\varrho c_V \nu l_{bulk})/3$. Equation 4.12 infers two things: First, a plot of the inverse of thermal conductivity obtained from the simulation, $1/\kappa_{MD}$ versus the inverse of simulation length, $1/L_z$ should be linear. Second, the thermal conductivity at bulk state, κ_{bulk} can be obtained as the inverse of y-intercept of the graph. Thus, the 'bulk' thermal conductivity can be derived by extrapolating the results of thermal conductivity to an infinite-size system.

Chapter 5

Results and Discussion

By carrying out the methods as described in Chapter 4, results of atomic behavior and thermodynamic properties are obtained and discussed in this Chapter.

5.1 Microscopic Behavior

Molecular dynamics simulations is not limited to evaluate the macroscopic thermodynamic properties, but is also powerful to understand the basic physics behind the macroscopic properties. In this section, results from atomic point of view are presented, including the interactions between atoms and the atomic radial distribution function.

5.1.1 Interatomic Potential

From the classical potentials which were developed in this study, the material's interatomic interactions can be studied, for example, we would like to know which

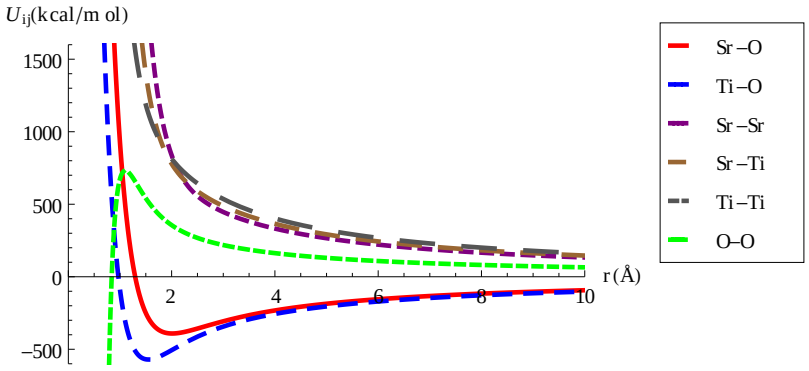

(a) $SrTiO_3$

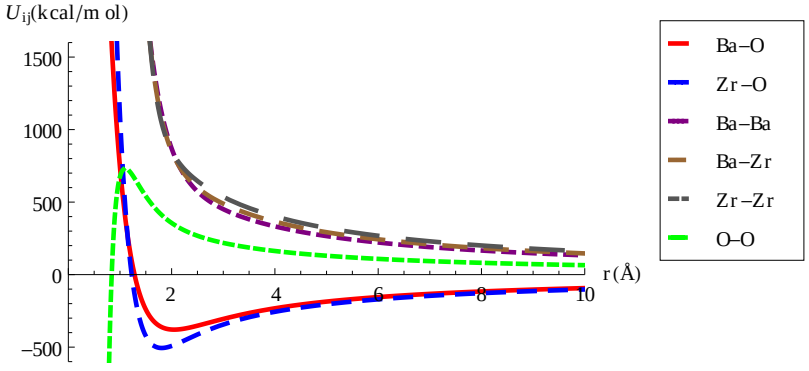

(b) $BaZrO_3$

FIGURE 5.1: Potential functions of $SrTiO_3$ and $BaZrO_3$.

components of the forces are responsible to bound the atoms together, or in other words, to form a bound state for the material.

In order to understand this, it is useful to plot each pairing potential, i.e. the potential between a pair of ions, based on Equation 4.1 and Table 4.1, and to locate for potential well. The interatomic potentials of $SrTiO_3$ and $BaZrO_3$ are shown in Figure 5.1. From the figure, it is manifest that only the potential of $Sr - O$, $Ti - O$, $Ba - O$ and $Zr - O$, where the ionic attraction is preponderant, show the typical potential well. It appears that these ionic potentials could support bound state due to the formation of the potential well.

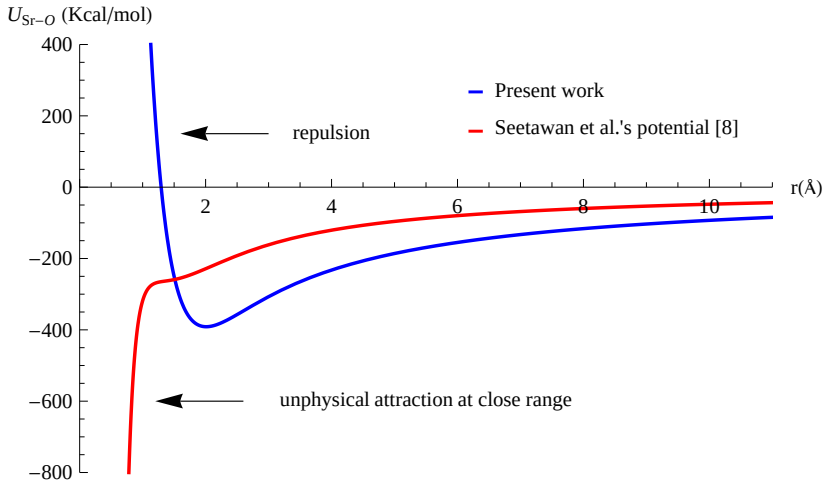

FIGURE 5.2: Seetawan *et al* 's potential [1] for Sr − O pair shows unphysical attraction at close range, whereas our potential shows repulsion.

5.1.2 Unphysical Attraction of Sr-O Potential

Despite the fact that obtaining a reliable interatomic potential is crucial in molecular dynamics simulation, error can still be found in the literature. In this section, I shall expound an error that has been pointed out by us.

For strontium titanate, there exist two well known sets of potential parameters, i.e. published by Katsumata *et al* [42] and Seetawan *et al* [1]. However, using the set of potential parameters published by Seetawan *et al* [1], lattice parameters as reported by them are unable to be reproduced at temperatures beyond 1200 K, though their lattice parameters are able to be reproduced at lower temperatures. Their potential parameters have been cafully analyzed.

Our analysis shows that the interacting potential between Sr − O in their potential parameters [1] has an unphysical attraction at close range (Figure 5.2), which causes the simulation to be unstable and results in particle lost. This unphysical close range attraction is the reason to the failure of the potential parameters published by them, i.e. to being unable to preserve the number of

particles in the simulation. This fatal inadvertence has not been pointed out by anyone before.

Our further analysis shows that, at lower temperatures, this effect has not been observed because other components of the potential parameters keep the atoms far apart that the chances of getting the atoms falling into the 'trap' are negligible and make the unphysical attraction to have no effect. Conversely, at higher temperatures, the particles have higher energy that the chances of getting Sr and O particles overlapping is higher.

It is not clear to us how Seetawan *et al* [1] were able to obtain the values of lattice parameter at temperatures beyond 1200 K, while at the same time, having an unphysical interaction in their potential. Initially when using the set of potential parameters published by Katsumata et al. [42], we failed to reproduce the lattice parameters as reported in their paper. Our analysis shows that this is because their values of Van der Waals attraction parameters C_i (i=Sr,Ti,O) are too small. After that we contacted them and they mentioned that the values are a factor of 1000 short and should be revised to $C_i \times 1000$. Now we are able to reproduce their lattice parameters. The fact that we are able to reproduce Katsumata *et al* [42] lattice parameters using their potential parameters even to elevated temperatures strengthens the case that Seetawan *et al* reproduction at high temperatures has been overlooked and is wrongly presented.

5.1.3 Radial Distribution Function

In order to gain a better understanding of the microscopic behavior of the perovskite materials, radial distribution functions of the system have been obtained

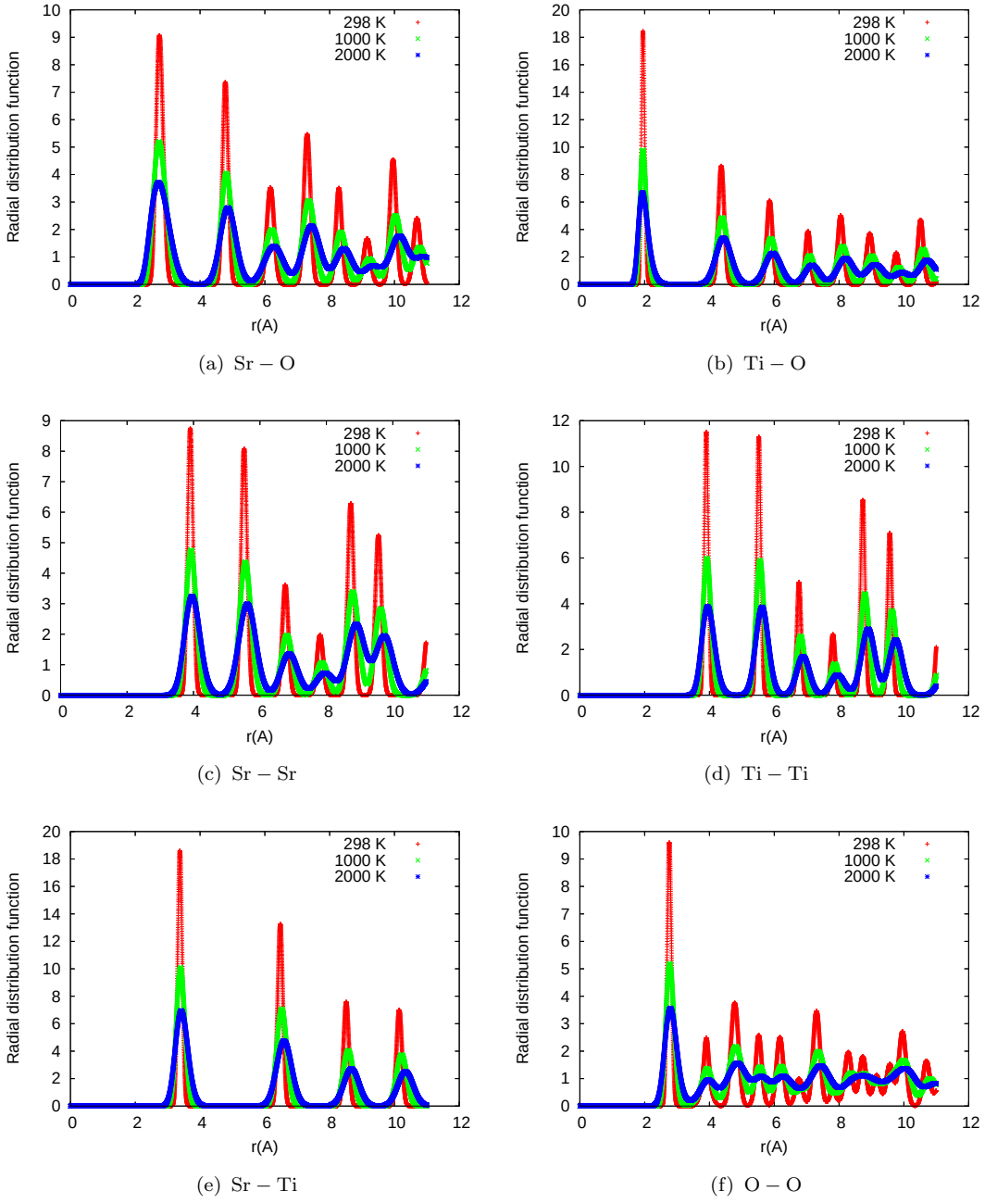

(a) Sr – O (b) Ti – O

(c) Sr – Sr (d) Ti – Ti

(e) Sr – Ti (f) O – O

FIGURE 5.3: Radial distribution function of $SrTiO_3$ at 298K (Red), 1000K (Green) and 2000K (Blue).

at temperatures of 298 K, 1000 K and 2000 K. The radial distribution functions obtained from the simulation are shown in Figure 5.3 and 5.4.

From the figures, it can be seen that the radial distribution functions show

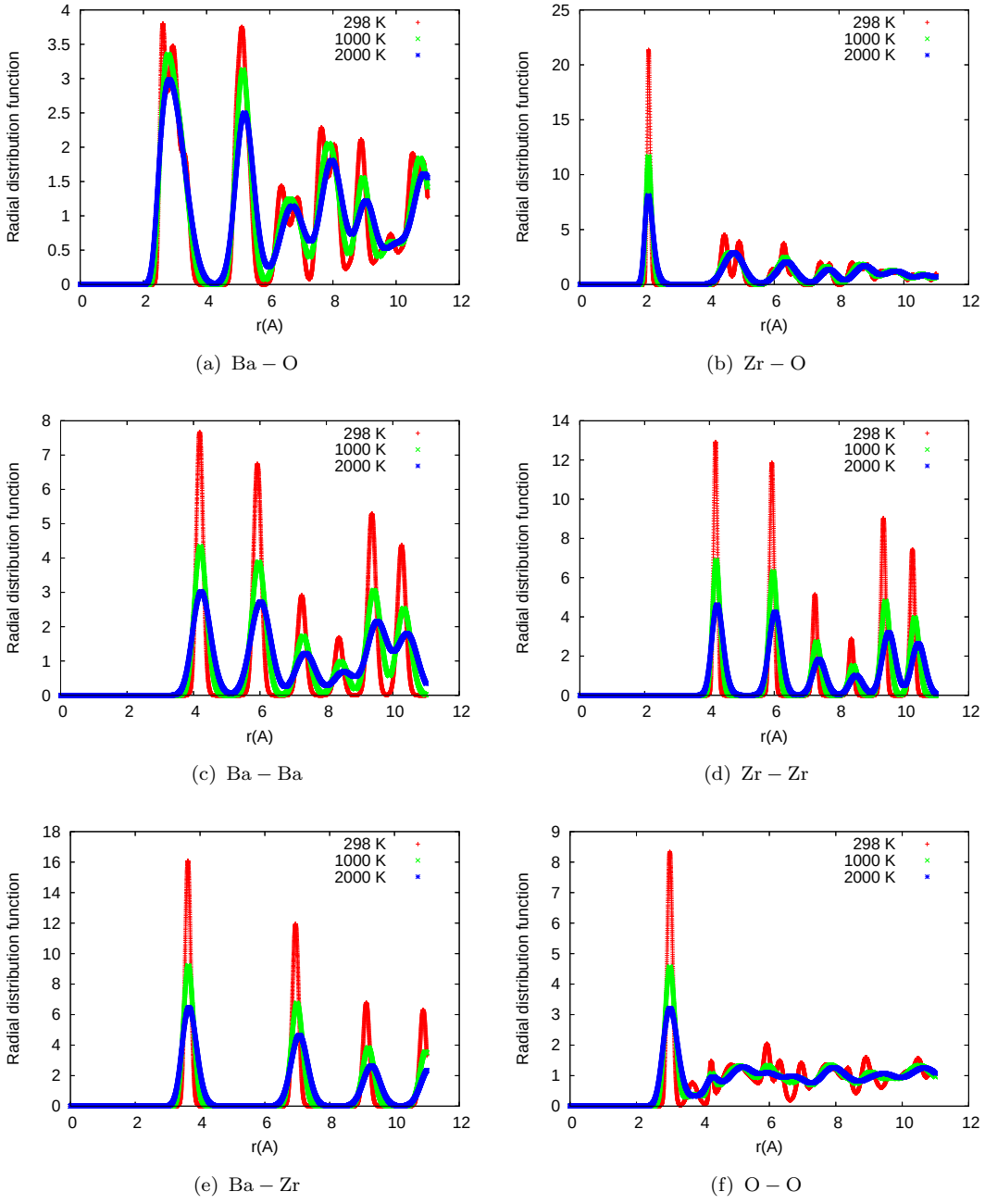

(a) Ba – O

(b) Zr – O

(c) Ba – Ba

(d) Zr – Zr

(e) Ba – Zr

(f) O – O

FIGURE 5.4: Radial distribution function of $BaZrO_3$ at 298K (Red), 1000K (Green) and 2000K (Blue).

sharp peaks at all three temperatures. These peaks reveal that the atoms in the system are closely packed, in other words, the system is in solid phase. Comparing between the radial distribution functions at different temperatures, the peaks at higher temperatures broaden out because the atoms vibrate with greater amplitudes. Notice that a single peak splitting into two peaks happens only for $BaZrO_3$ and is most obvious in Figure 5.4(a). This is a rare phenomena observed in the present study and point to some asymmetry. This phenomena has not been observed for $SrTiO_3$. Further works need to be done in order to gain a better understanding of this phenomena.

The radial distribution functions also reveal details about the interatomic seperation. For instance, the first peak of the radial distribution function of $Ti-O$ is located at 1.946 Å, which can be interpreted as the bond length of $Ti-O$. In fact, this value lies within the potential well of $Ti-O$, where the atoms are more likely to stay around. Table 5.1 shows the interatomic seperations and first coordination numbers of $SrTiO_3$ and $BaZrO_3$ at 298 K, 1000 K and 2000 K. The results of coordination numbers are confirmed by their perovskite structure. The coordination numbers of both materials remain the same for all three temperatures. This explains that the ceramic materials maintain their perovskite structures and did not undergo any dynamic transformation at high temperatures. This also infers that the materials are stable in the temperature range of 298 - 2000 K. Notice that some of the bond lengths, e.g. $Ti-O$, did not increase with temperatures or the increments are small. One of the possible explanations is that the other bond lengths, e.g. $Sr-Sr$, increase with temperature more than they should be, so the lattice constant can maintain the actual increment with temperature.

TABLE 5.1: Interatomic separation and first coordination numbers of $SrTiO_3$ and $BaZrO_3$ at 298 K, 1000 K and 2000 K.

(a) $SrTiO_3$

Pair	Interatomic separation/bond length (Å)			First coordination number		
	298 K	1000 K	2000 K	298 K	1000 K	2000 K
Sr – O	2.74945	2.73735	2.73185	12	12	12
Ti – O	1.94645	1.94095	1.92995	6	6	6
Sr – Sr	3.90115	3.92425	3.96165	6	6	6
Ti – Ti	3.90335	3.91655	3.93635	6	6	6
Sr – Ti	3.37865	3.39185	3.41385	8	8	8
O – O	2.76045	2.77805	2.78685	8	8	8

(b) $BaZrO_3$

Pair	Interatomic separation/bond length (Å)			First coordination number		
	298 K	1000 K	2000 K	298 K	1000 K	2000 K
Ba – O	2.61635	2.78355	2.82315	12	12	12
Zr – O	2.12245	2.11805	2.11695	6	6	6
Ba – Ba	4.18495	4.19375	4.23335	6	6	6
Zr – Zr	4.18605	4.20695	4.23335	6	6	6
Ba – Zr	3.62285	3.63715	3.66465	8	8	8
O – O	3.00465	3.00575	3.00685	8	8	8

5.2 Macroscopic Thermodynamic Properties

Using molecular dynamics simulation and the potential parameters presented in Table 4.1, macroscopic properties of strontium titanate and barium zirconate have been evaluated. The calculated thermodynamic properties include thermal expansion, isothermal compressibility, heat capacity and thermal transport properties.

5.2.1 Crystal Structure and Structural Parameters

From the simulation, strontium titanate and barium zirconate are observed to possess cubic structures (Figure 5.5) with lattice constant of 3.9051 Å and 4.1916

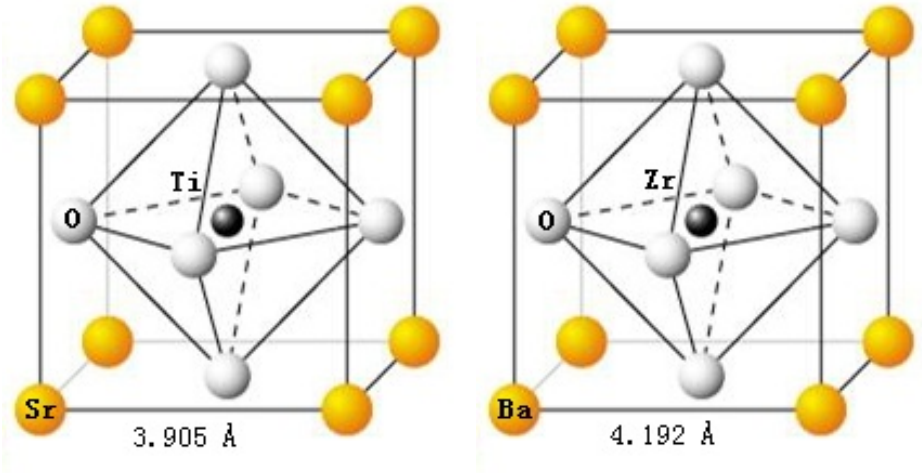

(a) $SrTiO_3$ (b) $BaZrO_3$

FIGURE 5.5: Crystal structures of $SrTiO_3$ and $BaZrO_3$. Pink=(Sr,Ba), Blue=(Ti,Zr) and Purple=O.

Å respectively at room temperature and ambient pressure. The lattice constant is regarded as the length of the simulation cell divided by the number of unit cells. The calculated lattice constants correspond well to the experimental values of 3.9051 Å [2] and 4.1918 Å [8].

TABLE 5.2: Structural parameters of $SrTiO_3$ and $BaZrO_3$ at 298 K and 1atm. a,b,c are the lattice constants, A,B,Γ are the angles and ϱ is the density.

	$SrTiO_3$		$BaZrO_3$	
Structural parameters	Present work	Experiment [2]	Present work	Experiment [8]
a (Å)	3.90516	3.9051	4.19167	4.1918
b (Å)	3.90509	3.9051	4.19148	4.1918
c (Å)	3.90516	3.9051	4.19152	4.1918
A (°)	90.00	90	90.01	90
B (°)	90.00	90	89.99	90
Γ (°)	90.00	90	90.00	90
ϱ (kg/m^3)	5116.09	5116.7	6235.88	6234.80[a]
Molar volume ($\times 10^{-5}$m^{3}mol^{-1})	3.5864	3.5863	4.4348	4.4356[a]

[a] Calculated from the experimental lattice parameter.

The structural parameters of $SrTiO_3$ and $BaZrO_3$ at 298 K and 1 atm, which were obtained from the simulation are shown in Table 5.2. It can be seen from the table that $BaZrO_3$ has larger lattice constants and molar volume compared with $SrTiO_3$. Since their atomic interactions are quite similar, including the magnitudes, as shown in Figure 5.1, one of the reasons why $BaZrO_3$ has a larger volume is that Ba^{2+} ion has a larger ionic radius than Sr^{2+} ion as the former has more electrons, and similarly Zr^{4+} ion has more electrons than Ti^{4+} ion and consequently a larger ionic radius, and this makes the ionic seperation in $BaZrO_3$ larger. Compared to the experimental results, the simulation results show excellent agreement.

5.2.2 Thermal Expansion

In order to study the materials' thermal behavior, the simulation has been extended to higher temperatures up to 2000 K. Lattice parameters and molar volumes of $SrTiO_3$ and $BaZrO_3$ have been calculated from 298 K to 2000 K with an increment of 100 K. The variation of lattice parameter and molar volume with temperature are shown in Figure 5.6 and Figure 5.7. From the simulation, the lattice parameter of $SrTiO_3$ increased monotonically from 3.9051 Å at 298 K to 3.9825 Å at 2000 K, and the lattice parameter of $BaZrO_3$ increased from 4.1916 Å at 298 K to 4.2676 Å at 2000 K. A third-order polynomial fitting to the lattice parameter of $SrTiO_3$ yields:

$$a(T)[\text{Å}] = 3.89 + 3.84 \times 10^{-5}T + 1.39 \times 10^{-9}T^2 + 8.15 \times 10^{-13}T^3 \qquad (5.1)$$

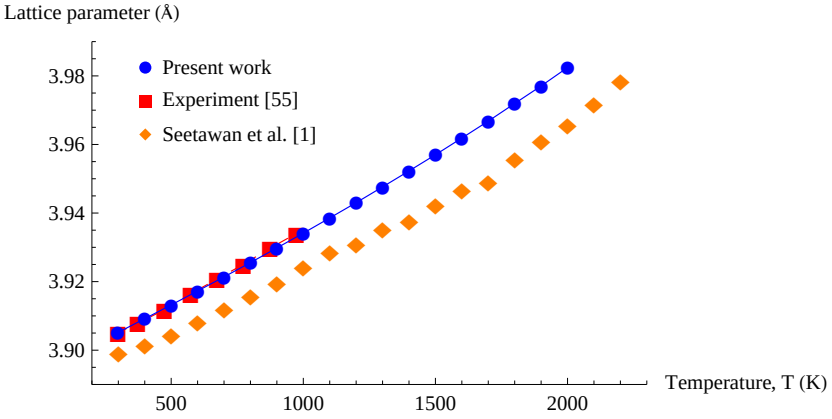

(a) $SrTiO_3$

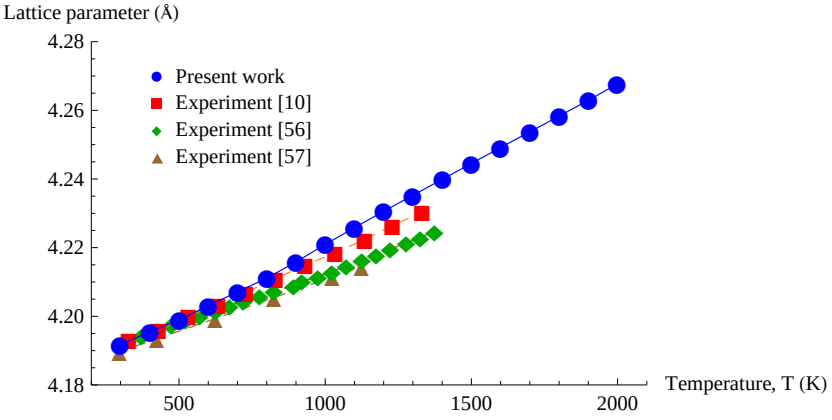

(b) $BaZrO_3$

FIGURE 5.6: Thermal variation of lattice parameters of $SrTiO_3$ and $BaZrO_3$.

and to the lattice parameter of $BaZrO_3$ yields:

$$a(T)[\mathring{\text{A}}] = 4.18 + 2.50 \times 10^{-5}T + 1.73 \times 10^{-8}T^2 - 4.35 \times 10^{-12}T^3 \qquad (5.2)$$

Compare against experimental data [10, 49–51], our results show good agreement. Although it is not clear to us that how Seetawan *et al* [1] obtained the values of lattice parameter of $SrTiO_3$ at temperature above 1200 K due to the unphysical

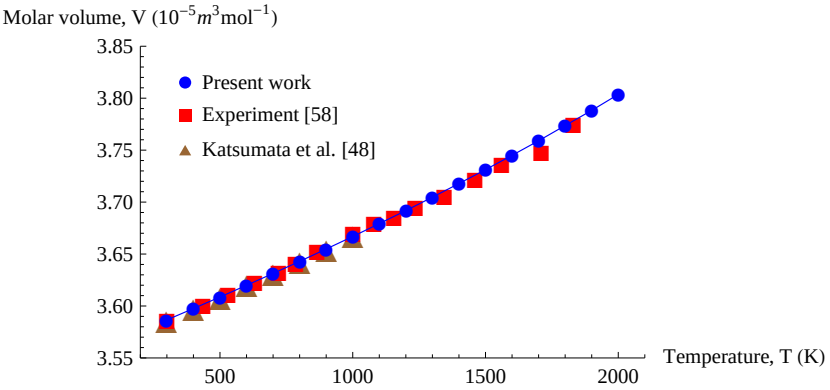

(a) $SrTiO_3$

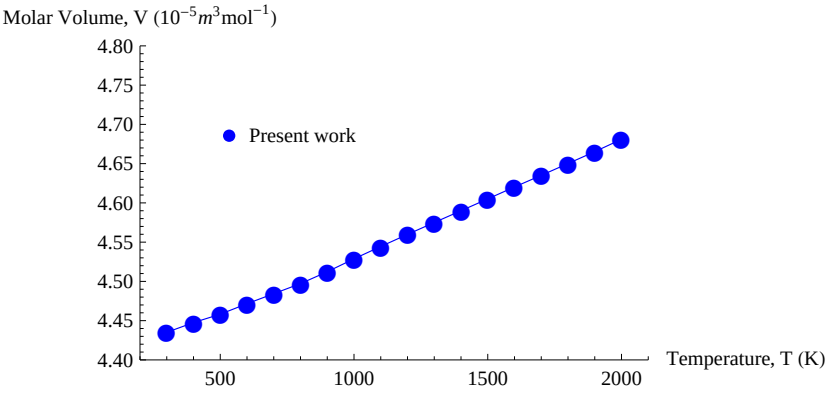

(b) $BaZrO_3$

FIGURE 5.7: Thermal variation of molar volumes of $SrTiO_3$ and $BaZrO_3$.

attraction of $Sr - O$ that they introduced, it is obvious from the figure that our result agrees better to the experimental values compared with theirs.

The molar volume of $SrTiO_3$ also increased, from 3.5864 $\times 10^{-5}$m^{3}mol^{-1} at room temperature to 3.8037 $\times 10^{-5}$m^{3}mol^{-1} at 2000 K, and the molar volume of $BaZrO_3$ shows increment as well from 4.4348 $\times 10^{-5}$m^{3}mol^{-1} at room temperature to 4.6807 $\times 10^{-5}$m^{3}mol^{-1} at 2000 K. It can be seen from the figure that our

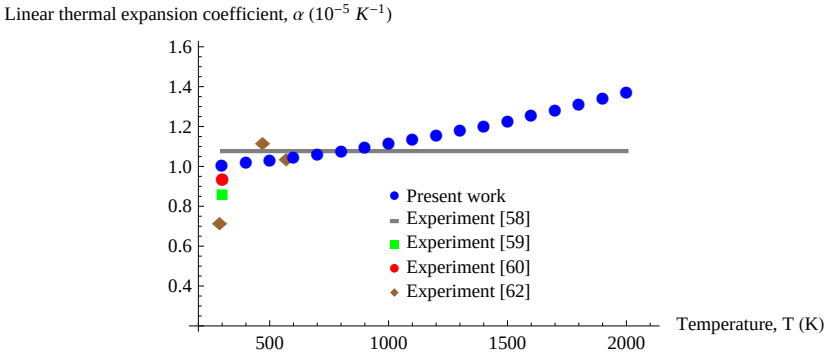

(a) $SrTiO_3$

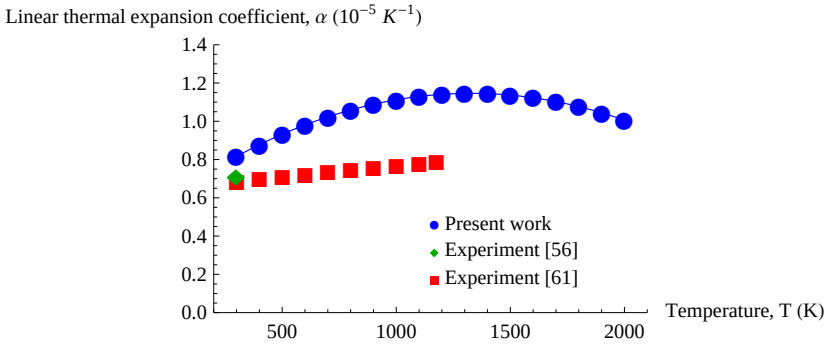

(b) $BaZrO_3$

FIGURE 5.8: Linear thermal expansion coefficients of $SrTiO_3$ and $BaZrO_3$ as a function of temperature.

simulation results agree very well with the experimental result of Ligny *et al* [52] and simulation results of Katsumata *et al* [42].

Linear thermal expansion coefficients, α of $SrTiO_3$ and $BaZrO_3$ derived according to equation 4.5 are shown in Figure 5.8. For $SrTiO_3$, the value of α at room temperature is calculated to be 1.010 $\times 10^{-5} K^{-1}$, and this value is compatible with the experimental values of 1.077 $\times 10^{-5} K^{-1}$ [52], 0.8630 $\times 10^{-5} K^{-1}$ [53]

and 0.9400 $\times 10^{-5}K^{-1}$ [54]. For $BaZrO_3$, the simulated and experimental values of α at room temperature are 0.8160 $\times$ 10^{-5} K^{-1} (present work), 0.7130 $\times$ 10^{-5} K^{-1} [50] and 0.6904 $\times$ 10^{-5} K^{-1} [55]. Thus, $SrTiO_3$ is slightly more expansible than $BaZrO_3$.

The experimental values [52–54, 56] of linear thermal expansion coefficient of $SrTiO_3$ are inconsistant as shown in Figure 5.8(a). While Ligny *et al* [52] deemed that it remains almost constant from room temperature up to 1800 K, our simulation suggests a diminutive growth from 1.010 $\times$ $10^{-5}K^{-1}$ at room temperature to 1.376 $\times 10^{-5}K^{-1}$ at 2000 K. For $BaZrO_3$, our simulation result, which shows increment from 0.816 $\times 10^{-5}K^{-1}$ at 298 K to 1.007 $\times 10^{-5}K^{-1}$ at 2000 K, agrees well with the experimental data [50, 55] at room temperature, but deviates at high temperatures.

5.2.3 Isothermal Compressibility

The materials' behavior under compression of high pressure was studied as well. As shown in Figure 5.9, the molar volumes of $SrTiO_3$ and $BaZrO_3$ decreased gradually from 3.586 $\times 10^{-5}m^3mol^{-1}$ at 1 atm to 3.247 $\times 10^{-5}m^3mol^{-1}$ at 20.3 GPa, and from 4.435 $\times$ 10^{-5} m^3 $mole^{-1}$ at 1 atm to 3.944 $\times$ 10^{-5} m^3 $mole^{-1}$ at 20.3 GPa respectively. The result of $SrTiO_3$ in the present study agrees remarkably well with the experimental findings [57, 58] and simulation result of Katsumata *et al* [42], whereas, for $BaZrO_3$, there are no existing data to compare with.

From the variation of volume with pressure, isothermal compressibility is derived according to Equation 4.6. At room temperature, isothermal compressibilities, β_T of $SrTiO_3$ and $BaZrO_3$ are calculated to be 5.800 $\times 10^{-12}Pa^{-1}$ and 7.338 $\times$ 10^{-12} Pa^{-1} respectively, and this infers that $SrTiO_3$ is less compressible than

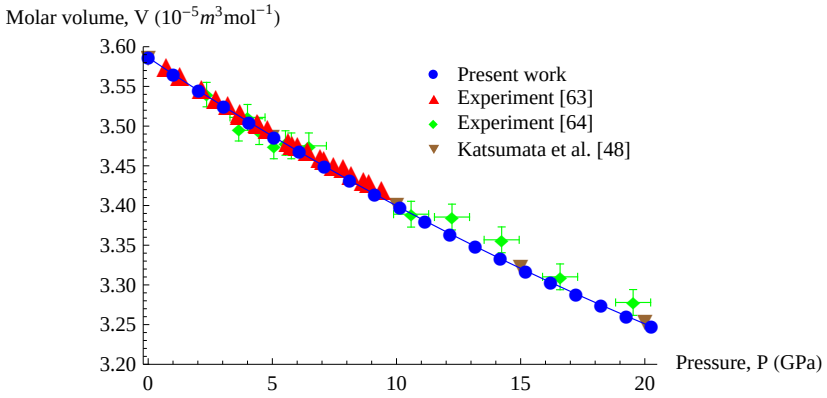

(a) $SrTiO_3$

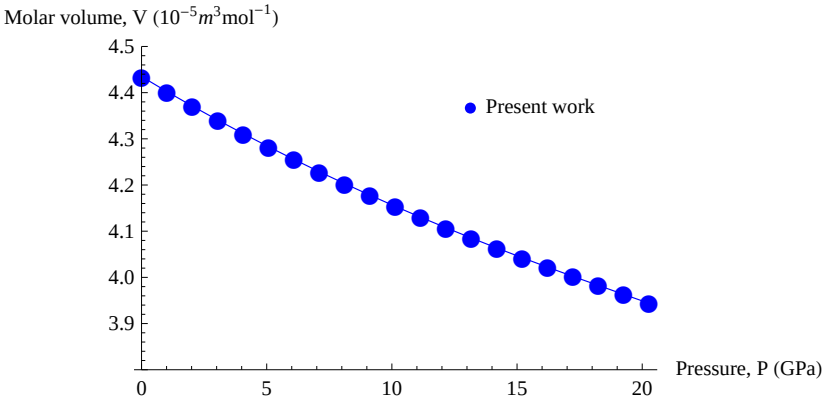

(b) $BaZrO_3$

FIGURE 5.9: Variation of molar volumes of $SrTiO_3$ and $BaZrO_3$ as a function of pressure.

$BaZrO_3$, in other words, $SrTiO_3$ is stiffer than $BaZrO_3$. The results predicted from the simulation are consistent with the experimental of 5.750 $\times 10^{-12}Pa^{-1}$ [3] for $SrTiO_3$ and 7.860 $\times 10^{-12}Pa^{-1}$ [50] for $BaZrO_3$ at room temperature.

Figures 5.10 and 5.11 show variation of isothermal compressibilities of $SrTiO_3$ and $BaZrO_3$ as a function of pressure and temperature. With increasing pressure, the values of isothermal compressibility of $SrTiO_3$ decreased from 5.800

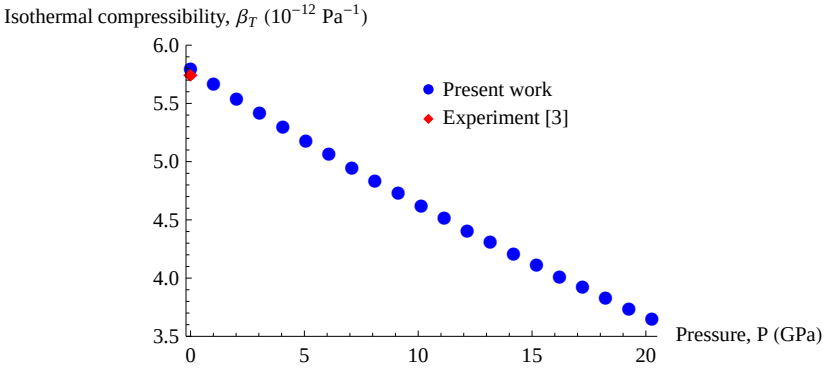

(a) $SrTiO_3$

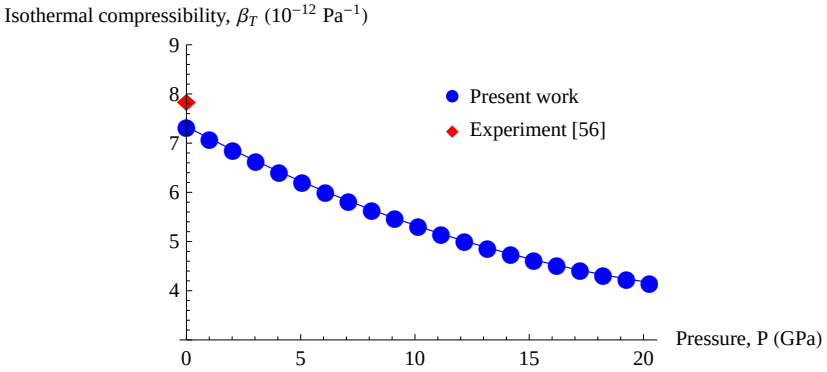

(b) $BaZrO_3$

FIGURE 5.10: Variation of isothermal compressibilities of $SrTiO_3$ and $BaZrO_3$ as a function of pressure at 298 K.

$\times 10^{-12} Pa^{-1}$ at ambient pressure to 3.658 $\times 10^{-12} Pa^{-1}$ at 20.3 GPa, and the values of isothermal compressibility of $BaZrO_3$ decreased from 7.338 $\times 10^{-12} Pa^{-1}$ at 1 atm to 4.167 $\times 10^{-12} Pa^{-1}$ at 20.3 GPa. Conversely, isothermal compressibilities of the materials increased with increasing temperature: $SrTiO_3$ approached 8.251 $\times 10^{-12} Pa^{-1}$ at 2000 K and $BaZrO_3$ impended 9.457 $\times 10^{-12} Pa^{-1}$ at 2000 K.

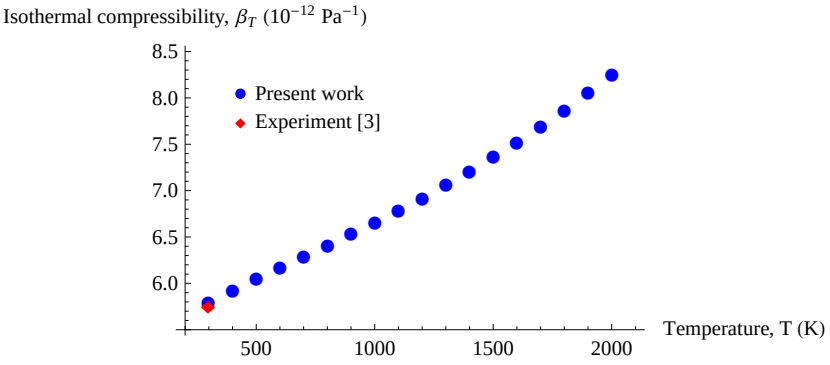

(a) $SrTiO_3$

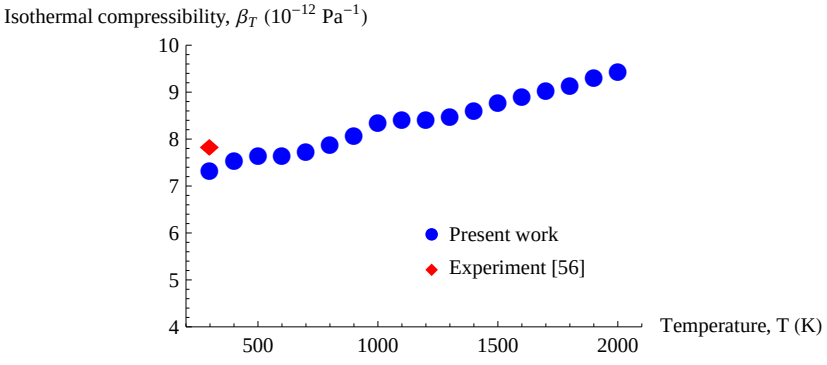

(b) $BaZrO_3$

FIGURE 5.11: Thermal variation of isothermal compressibilities of $SrTiO_3$ and $BaZrO_3$ at ambient pressure.

5.2.4 Heat Capacity

Heat capacity at constant pressure has been obtained from the atomic simulation based on the method described in Section 4.4.6. Figure 5.12 shows variation of constant-pressure heat capacities, C_P of $SrTiO_3$ and $BaZrO_3$ as a function of temperature.

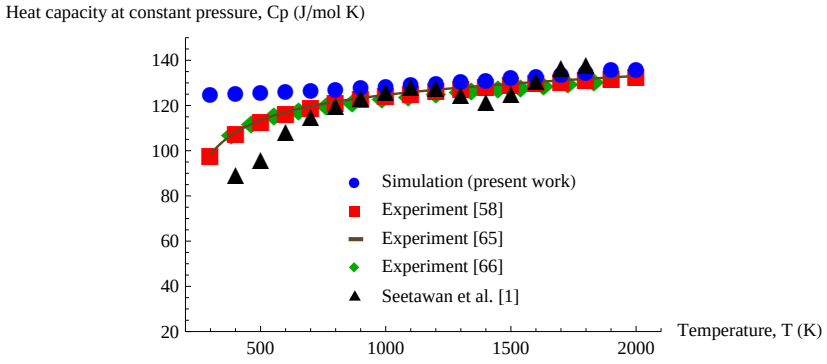

(a) $SrTiO_3$

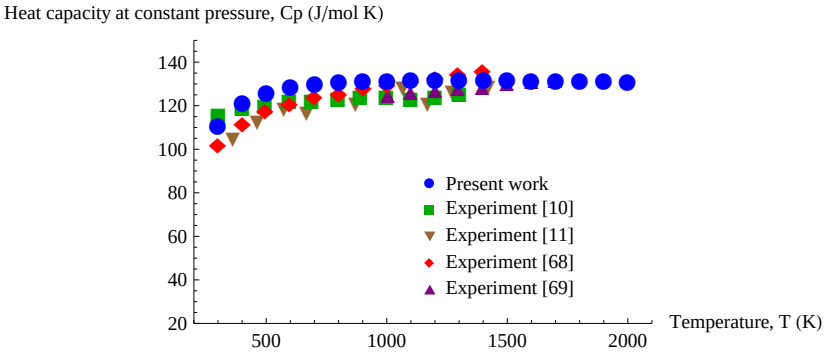

(b) $BaZrO_3$

FIGURE 5.12: Thermal variation of constant-pressure heat capacities of $SrTiO_3$ and $BaZrO_3$.

For $SrTiO_3$, the simulated heat capacity at constant pressure shows deviation from the experimental values [52, 59, 60] at lower temperatures, but corresponds well to the experimental results at temperatures above 700 K. Since the Debye temperature of $SrTiO_3$ is about 694 K [61], the simulation seems to work more efficient above the Debye temperature, and this can be understood in view of the classical basis of the program. The simulation result of Seetawan et al. [1] show

anomaly at temperature range around 1200 - 1600 K. They claimed that this is due to the material undergoes structural change from cubic to a tetragonal structure and then going back to the cubic structure at higher temperature. However, no evidence can confirm this anomaly. Our simulation result suggests no such transformation but a linear increase that is confirmed by the experiment.

For $BaZrO_3$, the simulated C_P is 110.8 J mol^{-1} K^{-1} at room temperature, which is consistent with the experimental values of 115.9 J mol^{-1} K^{-1} [10] and 102.4 J mol^{-1} K^{-1} [62]. At high temperatures, C_P shows good agreement with the variety of the experimental results [10, 11, 62, 63]. The trend of C_P as a function of temperature corresponds to the trend predicted based on the Debye model, which approaches Dulong-Petit limit above the Debye temperature. Worth mentioning that the Debye temperature of barium zirconate is 544 K [64]. An empirical equation of the temperature-dependent heat capacity of $BaZrO_3$ obtained in this study is given by:

$$C_P[\mathrm{Jmol^{-1}K^{-1}}] = 1.36 \times 10^2 - 2.08 \times 10^{-3}T - 2.19 \times 10^6 T^{-2} \tag{5.3}$$

5.2.5 Thermal Conductivity

Thermal transport properties of $SrTiO_3$ and $BaZrO_3$ have been studied using non-equilibrium molecular dynamics method[1] (NEMD) as described in Section 4.4.7.1, in which the kinetic energies are exchanged between the first bin and the middle bin of the simulation cell, and the temperature gradient, which is generated as a result of these energy exchanges, is measured. The thermal conductivity is then

[1]This method is implemented in LAMMPS [45].

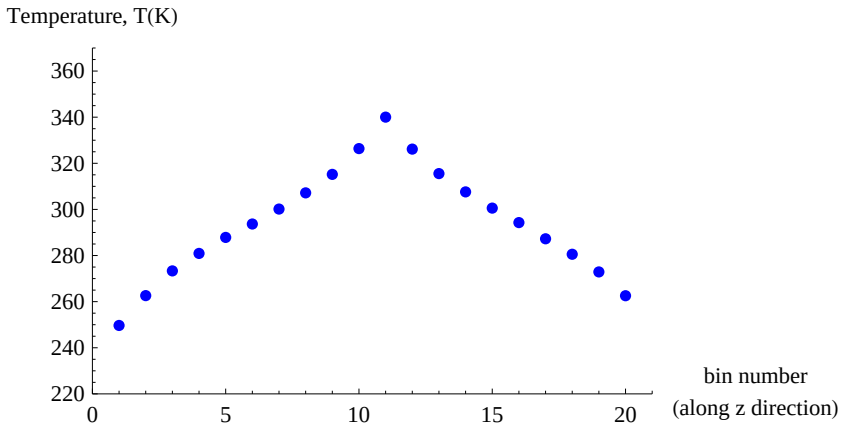

FIGURE 5.13: Averaged temperature gradient for $3 \times 3 \times 60$ unit cell of $SrTiO_3$ at 298K using exchange rates of 150 time steps.

calculated as the ratio of the total heat flux transferred and the temperature gradient.

In this study, kinetic energy exchange rates between 90 and 210 time steps were found to produce fairly linear temperature gradients for both systems. Hence, kinetic energy swap rate of 150 time steps has been chosen to induce linear temperature gradients. The mean temperature gradient of a $3 \times 3 \times 60$ unit cell $SrTiO_3$ system using exchange rates of 150 time steps as shown in Figure 5.13 is quite linear.

Instantaneous heat flux and thermal conductivity as a function of time for $SrTiO_3$ of $3 \times 3 \times 60$ unit cell at 298 K are shown in Figure 5.14. Obviously, the instantaneous thermal conductivity converged at 0.3 ns or 300,000 time steps. Therefore, the values of thermal conductivity of the first 300,000 time steps were ignored, and the heat energy transferred were accumulated for 3,000,000 time steps.

Phonon scatterings at the system boundaries give rise to finite size effect is non-negligible in molecular dynamics, if the simulation length is not significantly larger than the phonon mean free path. In order to account for this problem,

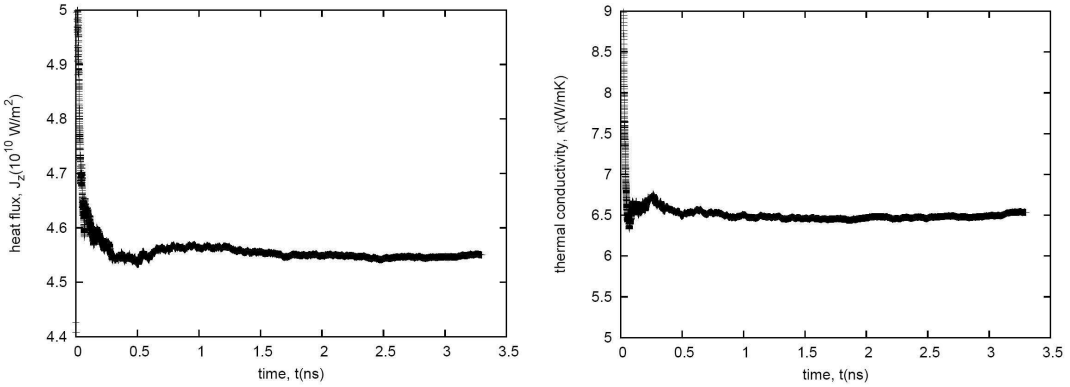

(a) Instantaneous heat flux (b) Instantaneous thermal conductivity

FIGURE 5.14: Instantaneous heat flux and thermal conductivity as a function of time for $3 \times 3 \times 60$ unit cell of $SrTiO_3$ at 298 K.

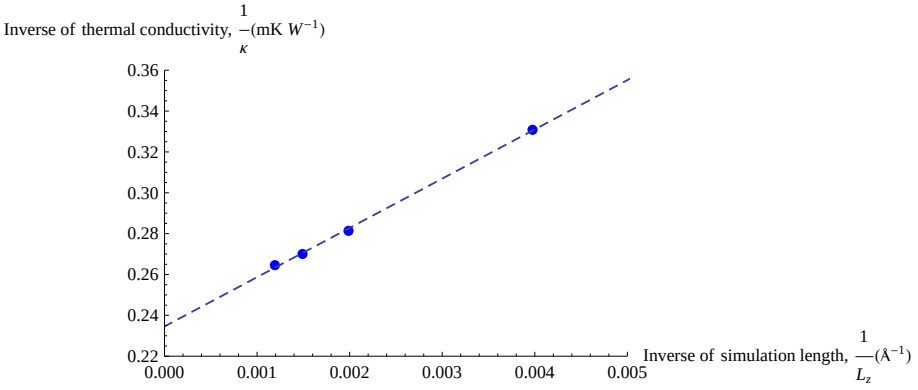

FIGURE 5.15: Inversed thermal conductivity as a function of inversed simulation length at 298 K for $BaZrO_3$. Extrapolation of the results to infinite-size system, i.e. $1/L_z = 0$, yields the bulk thermal conductivity.

corrections for the finite size effects have been made for both systems as described in Section 4.4.7.2.

Figure 5.15 shows inversed thermal conductivity as a function of inversed simulation length at 298 K for $BaZrO_3$ system of size $3 \times 3 \times N_z$ unit cell, where $N_z = 60, 120, 160, 200$. The gradient shown in the figure is linear, and hence, this is consistent with the inference of Equation 4.12. The y-intercept, which is the inversed thermal conductivity is obtained to be 0.235 m K W^{-1}. Therefore, the value of thermal conductivity of $BaZrO_3$ at room temperature is 4.26 W m^{-1}

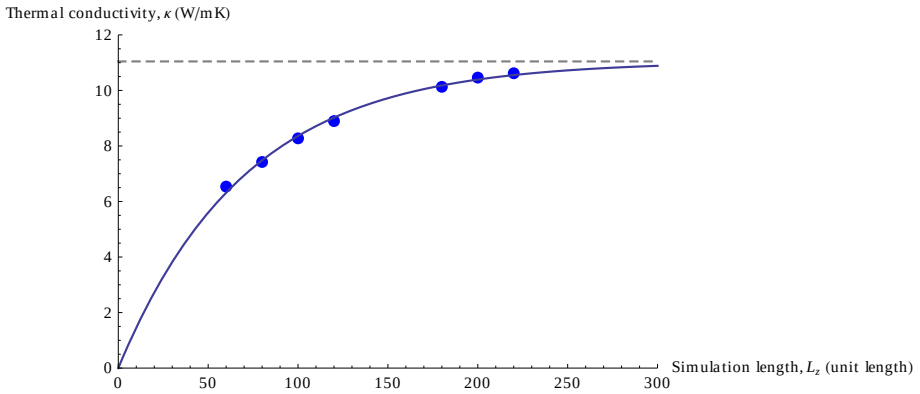

FIGURE 5.16: Thermal conductivity as a function of simulation length of $SrTiO_3$ at room temperature. The dashed line is the limit of the fitting function.

K^{-1}, which is consistent with the experimental value of Vassen *et al* [10] of about 4.31 W m^{-1} K^{-1}.

Besides using the method as described in Section 4.4.7.2, an alternative method to correct for the finite size effects is proposed. To illustrate this method, $SrTiO_3$ is used as an example. Thermal conductivity calculations were carried out on simulation cells of size $3 \times 3 \times N_z$ unit cell, where $N_z = 60, 80, 100, 120, 180, 200, 220$. The result as a function of simulation length is shown in Figure 5.16. It can be seen from the figure that the thermal conductivity increased exponentially with incresing simulation length, and the values converged at large simulation length. Since the exponential trend is quite similar to that of charging a capacitor in RC cricuit or the effect of an inductance to currect in RL circuit, so a function of the form

$$f(L_z) = \epsilon(1 - e^{-L_z/\lambda}) \tag{5.4}$$

where ϵ and λ are fitting parameters, can be fitted through the points as shown in Figure 5.16. It can be seen from the figure that it has been fitted quite well (solid line). Thus, the saturation limit of the fitting function gives thermal conductivity in the bulk state, which is at infinite length, and this method also eliminates the

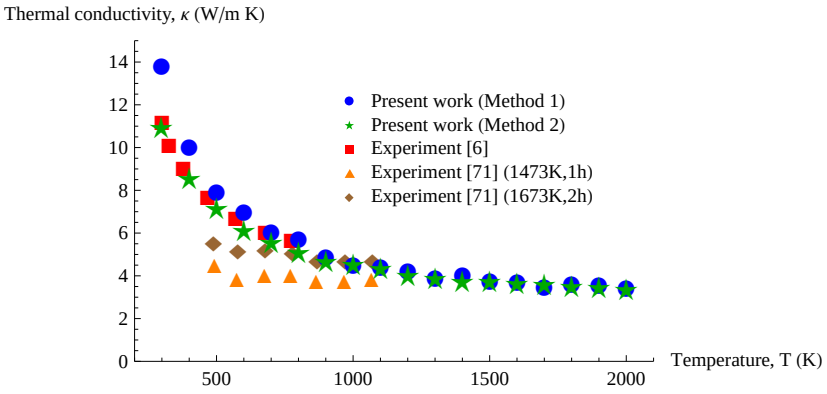

(a) $SrTiO_3$

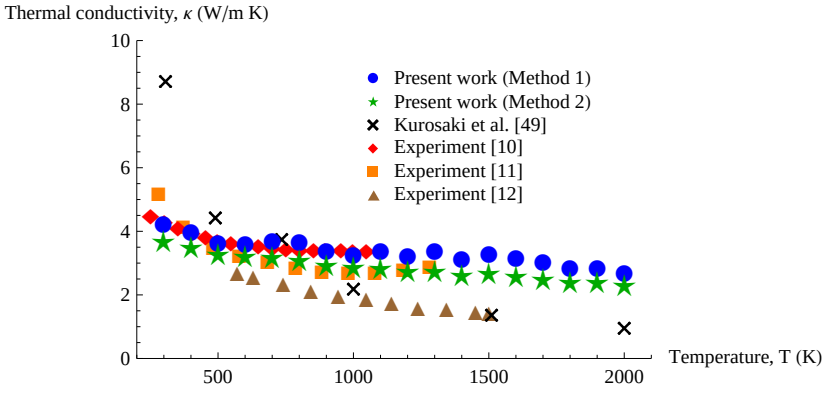

(b) $BaZrO_3$

FIGURE 5.17: Variation of 'bulk' thermal conductivity of $SrTiO_3$ and $BaZrO_3$ as a function of temperature. Method 1 used Equation 4.12 to correct for the finite size effects as described in Section 4.4.7.2, whereas method 2 adopted Equation 5.4.

finite size effect due to phonon scattering at the boundaries.

Thermal conductivities of $SrTiO_3$ and $BaZrO_3$ with corrections made for finite size effects are shown in Figure 5.17. Notice that method 1 refers to the correctional method as described in Section 4.4.7.2, whereas method 2 used Equation 5.4 to correct for the finite size effects. If comparing between both correctional

methods, it can be seen that even though the results obtained using method 2 are slightly lower that that of method 1, in overall, they are quite similar. The discussions of thermal conductivities of $SrTiO_3$ and $BaZrO_3$ are broke down into three parts, where the result of $SrTiO_3$ is discussed first, and then followed by the result of $BaZrO_3$, and lastly the comparison between the thermal conductivities of both materials.

Figure 5.17(a) shows variation of 'bulk' thermal conductivity of $SrTiO_3$ as a function of temperature. Notice that the two experimental values of the thermal conductivity are inconsistent. From kinetic theory, thermal conductivity as a function of temperature should follows the trend of $1/T^{\eta}$ at high temperatures, where η has a value between 1 and 2. The experimental values from Muta at al. [6] fulfilled this trend, but the experimental values from Ito et al. [65] showed almost constant values with increasing temperature. Our simulation result obtained using NEMD method shows declination with increasing temperature and follows the trend of $1/T^{\eta}$. Using correctional method 1, the result shows declination from 11.04 W/mK at room temperature to 3.485 W/mK at 2000 K, and using correctional method 2, the values decreased from 13.84 W/mK at room temperature to 3.456 W/mK at 2000 K. These results agree very well with the experimental values obtained from Muta et al. [6].

The thermal conductivity of $BaZrO_3$ with corrections made for the finite size effects is shown in Figure 5.17(b), together with the experimental data [10–12]. The thermal conductivity obtained from the simulation demonstrates a descending trend from 4.263 W m^{-1} K^{-1} at room temperature to 2.720 W m^{-1} K^{-1} at 2000 K using correctional method 1, and from 3.758 W m^{-1} K^{-1} at room temperature to 2.371 W m^{-1} K^{-1} at 2000 K using correctional method 2. The result matches with the experimental values obtained from Vassen *et al* [10] very well.

Compared with simulation result of Kurosaki *et al* [43], it is evident from the figure that our interatomic potential works better.

Comparing between the thermal conductivities of $SrTiO_3$ and $BaZrO_3$, it can be seen from Figure 5.17 that $SrTiO_3$ has a higher value of thermal conductivity than $BaZrO_3$. This infers that the former should has a higher Debye temperature than the latter, and thus, $SrTiO_3$ should be stiffer than $BaZrO_3$. In other words, $SrTiO_3$ should has a lower isothermal compressibility value. In fact, this has been confirmed by our simulation result of isothermal compressibilities of $SrTiO_3$ and $BaZrO_3$ (Section 5.2.3), which yields a value of 5.80 $\times 10^{-12} Pa^{-1}$ for $SrTiO_3$ and 7.34 $\times 10^{-12} Pa^{-1}$ for $BaZrO_3$. Furthermore, the Debye temperature of $SrTiO_3$ and $BaZrO_3$ are 694 K [61] and 544 K [64] respectively, which again confirmed the results of thermal conductivities of $SrTiO_3$ and $BaZrO_3$.

Chapter 6

Conclusion

Molecular dynamics simulation has been carried out on strontium titanate and barium zirconate perovskite materials in order to study their microscopic behavior, such as the interatomic interactions and radial distribution function, and to obtain the macroscopic thermodynamic properties, including the structural parameters, thermal expansion coefficient, isothermal compressibility, heat capacity and thermal transport property. Conclusions that have been reached are shown below:

1. New sets of potential parameters of $SrTiO_3$ and $BaZrO_3$ have been derived and implemented, and the accuracies of the potentials have been justified by comparing against the experimental findings.

2. Radial distribution functions of $SrTiO_3$ and $BaZrO_3$ reveal that the solid perovskite compounds did not undergo dynamical structural change at high temperatures, and stabilities of the materials have been achieved at 298 - 2000 K.

3. Lattice parameters, molar volumes, thermal expansion coefficient and isothermal compressibility have been evaluated in the temperature range of 298 K to 2000 K and pressure ranging from 1 atm to 20.3 GPa. These calculated thermodynamic properties are found to be compatible with the experimental results.

4. The heat capacity at constant pressure of $SrTiO_3$ obtained from the simulation did not show anomaly at high temperatures, which was introduced in the simulation result of Seetawan *et al* [1]. Conversely, it agrees with the experimental values. The heat capacity at constant pressure of $BaZrO_3$ not only agrees with the experimental data, but also corresponds to the trend predicted based on Debye model.

5. Thermal transport properties of $SrTiO_3$ and $BaZrO_3$ have been studied in the temperature range from room temperature to 2000 K using NEMD method. Corrections for the finite size effect based on two methods have been made, and the results did not deviate much. The simulation results of thermal conductivities show excellent agreement with the experimental findings.

Therefore, it can be concluded that the molecular dynamics simulation and the new interatomic potential parameters are successful in studying the atomic behavior and obtaining the physical, thermodynamic and thermal transport properties of $SrTiO_3$ and $BaZrO_3$ perovskite materials.

Chapter 7

Recommendations

A few recommendations for further study are described below.

1. This study has used strontium titanate and barium zirconate perovskite materials as examples to simulate their thermodynamic and thermal transport properties. Therefore, similar simulation can be carried out on other materials of interest, but not necessary limited to perovskite-type compounds. On the other hand, since most of the important thermodynamic properties of $SrTiO_3$ and $BaZrO_3$ have been investigated, this work can be extended to study for other phenomena, such as phase transition, in which more accurate potential, such as the inclusion of three-body potential [29] is required.

2. Molecular dynamics simulation is almost impeccable, except for a few limitations associated with the classical simulation:

   i) Empirical inputs are required.

   One of the drawbacks of the classical simulation is that experimental inputs for the potential parametrization are required. For instance, when

parametrizing the potential for $BaZrO_3$ system, knowledge on some of the experimental physical properties, such as lattice parameters, thermal expansion and isothermal compressibility are required. The higher the accuracy of the potential one desired, the more experimental inputs are required. On the other hand, ab-initio parametrization, which based on density functional theory, is able to solve this problem; it does not required prior knowledge on the physical properties or the experimental data. Thus, it is a powerful method to design novel materials. Furthermore, it is also a notable technique to study the material's behavior from the atomic point of view.

ii) Electronic properties cannot be revealed.

It is understood that molecular dynamics simulation, which is based on solving the classical equation of motions, reveal no information about the electronic properties of the materials. In other words, it is impossible to study, for example, electronic band structure of a material. Hence, more advanced technique is required in order to gain a better understanding of the materials of interest. First-principles calculation based on density functional theory or Monte Carlo method has overcome this problem. Tons of literatures pertaining to the first-principles method can be found. For example, the electronic properties of Struvite have been studied by Romanowski *et al* [66] using the density functional theory approach. Therefore, first-principles study of the perovskite materials is proposed to extend this work.

References

[1] T. Seetawan, G. Wong-ud-dee, C. Thanachayanont, and V. Amornkitbumrung. Molecular dynamics simulation of strontium titanate. *Chinese Physics Letters*, 27(2):026501, 2010.

[2] R. W. G. Wyckoff. *Crystal Structures*. John Wiley and Sons, New York Sons, New York, 1964.

[3] R. O. Bell and G. Rupprecht. Elastic constants of strontium titanate. *Phys. Rev.*, 129:90–94, Jan 1963.

[4] P. Blennow, Anke Hagen, K. K. Hansen, L. R. Wallenberg, and M. Mogensen. Defect and electrical transport properties of Nb-doped $SrTiO_3$. *Solid State Ionics*, 179(35-36):2047 – 2058, 2008.

[5] H. Muta, K. Kurosaki, and S. Yamanaka. Thermoelectric properties of doped $BaTiO_3 - SrTiO_3$ solid solution. *Journal of Alloys and Compounds*, 368(1-2):22 – 24, 2004.

[6] H. Muta, K. Kurosaki, and S. Yamanaka. Thermoelectric properties of reduced and La-doped single-crystalline $SrTiO_3$. *Journal of Alloys and Compounds*, 392(1-2):306 – 309, 2005.

[7] D. J. Cumming, J. A. Kilner, and S. Skinner. Structural properties of Ce-doped strontium titanate for fuel cell applications. *J. Mater. Chem.*, 21(13): 5021–5026, 2011.

[8] I. Charrier-Cougoulic, T. Pagnier, and G. Lucazeau. Raman spectroscopy of perovskite-type $BaCe_xZr_{1-x}O_3 (0 \leq x \leq 1)$. *Journal of Solid State Chemistry*, 142(1):220 – 227, 1999.

[9] I. El-Harrad and A. Ridah. Composition-temperature phase diagram for barium-doped lead zirconate ferroelectric ceramics determined by raman spectroscopy. *Moroccan Journal of Condensed Matter*, 12(2), 2010.

[10] R. Vassen, X. Cao, F. Tietz, D. Basu, and D. Stöver. Zirconates as new materials for thermal barrier coatings. *Journal of the American Ceramic Society*, 83(8):2023–2028, 2000.

[11] S. Yamanaka, T. Hamaguchi, T. Oyama, T. Matsuda, S. Kobayashi, and K. Kurosaki. Heat capacities and thermal conductivities of perovskite type $BaZrO_3$ and $BaCeO_3$. *Journal of Alloys and Compounds*, 359(12):1 – 4, 2003.

[12] P. S. Murti and M. V. Krishnaiah. Thermal diffusivity and thermal conductivity studies on the zirconate, cerate and uranate of barium. *Journal of Thermal Analysis and Calorimetry*, 37(11):2643–2648, 1991.

[13] J. H. Shim, J. S. Park, J. An, T. M. Gur, S. Kang, and F. B. Prinz. Intermediate-temperature ceramic fuel cells with thin film yttrium-doped barium zirconate electrolytes. *Chemistry of Materials*, 21(14):3290–3296, 2009.

[14] H. Kaburaki, J. L., S. Yip, and H. Kimizuka. Dynamical thermal conductivity of argon crystal. *Journal of Applied Physics*, 102(4):043514, 2007.

[15] A. D. MacKerell, D. Bashford, Bellott, R. L. Dunbrack, J. D. Evanseck, M. J. Field, S. Fischer, J. Gao, H. Guo, S. Ha, D. Joseph-McCarthy, L. Kuchnir, K. Kuczera, F. T. K. Lau, C. Mattos, S. Michnick, T. Ngo, D. T. Nguyen, B. Prodhom, W. E. Reiher, B. Roux, M. Schlenkrich, J. C. Smith, R. Stote, J. Straub, M. Watanabe, J. Wirkiewicz-Kuczera, D. Yin, and M. Karplus. All-atom empirical potential for molecular modeling and dynamics studies of proteins. *The Journal of Physical Chemistry B*, 102(18):35863616, 1998.

[16] A. D. Bobadilla and J. M. Seminario. DNA-CNT interactions and gating mechanism using MD and DFT. *The Journal of Physical Chemistry C*, 115 (8):34663474, 2011.

[17] S. Jayaraman, A. P. Thompson, O. A. von Lilienfeld, and E. J. Maginn. Molecular simulation of the thermal and transport properties of three alkali nitrate salts. *Industrial & Engineering Chemistry Research*, 49(2):559571, 2010.

[18] Q.B. Fan, F. Zhang, F.Z. Wang, and L. Wang. Molecular dynamics calculation of thermal expansion coefficient of a series of rare-earth zirconates. *Computational Materials Science*, 46(3):716 – 719, 2009.

[19] M. Matsui. Molecular dynamics study of $MgSiO_3$ perovskite. *Physics and Chemistry of Minerals*, 16:234–238, 1988.

[20] M. Matsui. Molecular dynamics simulation of $MgSiO_3$ perovskite and the 660-km seismic discontinuity. *Physics of the Earth and Planetary Interiors*, 121(12):77 – 84, 2000.

[21] A. Yokoi, H. Masumoto, and J. Sugishita. Phase transitioncrystal structure relations in ferroelectric $Bi_{2.5}Na_{1.5}Nb_3O_{12}$ compound by molecular dynamics simulation. *Materials Chemistry and Physics*, 116(1):16 – 20, 2009.

[22] K. Kurosaki, M. Imamura, I. Sato, T. Namekawa, M. Uno, and S. Yamanaka. Molecular dynamics studies of neptunium dioxide. *Journal of Alloys and Compounds*, 387(12):9 – 14, 2005.

[23] C.B. Basak, A.K. Sengupta, and H.S. Kamath. Classical molecular dynamics simulation of UO_2 to predict thermophysical properties. *Journal of Alloys and Compounds*, 360(12):210 – 216, 2003.

[24] S.K. Chien, Y.T. Yang, and C.K. Chen. Thermal conductivity and thermal rectification in carbon nanotubes with geometric variations of doped nitrogen: Non-equilibrium molecular dynamics simulations. *Physics Letters A*, 374(48):4885 – 4889, 2010.

[25] C.H. Wu and J.Y. Hsu. Thermal conductivity of carbon nanotubes with quantum correction via heat capacity. *Nanotechnology*, 20(14):145401, 2009.

[26] M. S. Daw and M. I. Baskes. Semiempirical, quantum mechanical calculation of hydrogen embrittlement in metals. *Phys. Rev. Lett.*, 50:1285–1288, Apr 1983.

[27] A.E. Gheribi. Molecular dynamics study of stable and undercooled liquid zirconium based on meam interatomic potential. *Materials Chemistry and Physics*, 116(23):489 – 496, 2009.

[28] A. C. T. van Duin, S. Dasgupta, F. Lorant, and W. A. Goddard. Reaxff: A reactive force field for hydrocarbons. *The Journal of Physical Chemistry A*, 105(41):93969409, 2001.

[29] R. A Jackson and M. E G Valerio. A new interatomic potential for the ferroelectric and paraelectric phases of $LiNbO_3$. *Journal of Physics: Condensed Matter*, 17(6):837, 2005.

[30] K. Amara, B. Soudini, D. Rached, and A. Boudali. Molecular dynamics simulations of the structural, elastic and thermodynamic properties of cubic bbi. *Computational Materials Science*, 44(2):635 – 640, 2008.

[31] Y G Xu and G R Liu. Fitting interatomic potentials using molecular dynamics simulations and inter-generation projection genetic algorithm. *Journal of Micromechanics and Microengineering*, 13(2):254, 2003.

[32] L. Angibaud, L. Briquet, P. Philipp, T. Wirtz, and J. Kieffer. Parameter optimization in molecular dynamics simulations using a genetic algorithm. *Nuclear Instruments and Methods in Physics Research Section B: Beam Interactions with Materials and Atoms*, 269(14):1559 – 1563, 2011.

[33] E G Maksimov, V I Zinenko, and N G Zamkova. Ab initio calculations of the physical properties of ionic crystals. *Physics-Uspekhi*, 47(11):1075, 2004.

[34] M.P. Allen. Introduction to molecular dynamics simulation. *Computational Soft Matter: From Synthetic Polymers to Proteins*, 23:1–28, 2004.

[35] T.-C. Lim. Connection among classical interatomic potential functions. *Journal of Mathematical Chemistry*, 36:261–269, 2004.

[36] T.-C. Lim. The relationship between lennard-jones (12-6) and morse potential functions. *Z. Naturforsch.*, 58 A:615–617, 2003.

[37] L. Verlet. Computer "experiments" on classical fluids. i. thermodynamical properties of lennard-jones molecules. *Phys. Rev.*, 159:98–103, Jul 1967.

[38] H. Sun. Compass: An ab initio force-field optimized for condensed-phase applicationsoverview with details on alkane and benzene compounds. *The Journal of Physical Chemistry B*, 102(38):73387364, 1998.

[39] D. Frenkel and B. Smit. *Understanding Molecular Simulation: From Algorithms to Applications*. Computational Science. San Diego: Academic Press, 2002.

[40] T. Schneider and E. Stoll. Molecular-dynamics study of a three-dimensional one-component model for distortive phase transitions. *Phys. Rev. B*, 17: 1302–1322, Feb 1978.

[41] K. Kawamura. Interatomic potential models for molecular dynamics simulations of multi-component oxides. *Springer Series in Solid-State Sciences*, 103:88–97, 1992.

[42] T. Katsumata, Y. Inaguma, M. Itoh, and K. Kawamura. Molecular dynamics simulation in $SrTiO_3$. *Solid State Ionics*, 108(14):175 – 178, 1998.

[43] K. Kurosaki, J. Adachi, T. Maekawa, and S. Yamanaka. Thermal conductivity analysis of $BaUO_3$ and $BaZrO_3$ by semiempirical molecular dynamics simulation. *Journal of Alloys and Compounds*, 407(12):49 – 52, 2006.

[44] D.C. Rapaport. *The Art of Molecular Dynamics Simulation*. Cambridge University Press, 2004.

[45] S. Plimpton. Fast parallel algorithms for short-range molecular dynamics. *Journal of Computational Physics*, 117(1):1 – 19, 1995.

[46] K. K. and K. Hirao. Material design using personal computer. *Shokabo Inc*, 1994.

[47] F. Müller-Plathe. A simple nonequilibrium molecular dynamics method for calculating the thermal conductivity. *J. Chem. Phys.*, 106(14):6082–6085, 1997.

[48] H. J., E. M. Myshakin, K. D. Jordan, and R. P. Warzinski. Molecular dynamics simulations of the thermal conductivity of methane hydrate. *The Journal of Physical Chemistry B*, 112(33):10207–10216, 2008.

[49] E. N. Bunting, G. R. Shelton, and A. S. Creamer. Properties of barium-strontium titanate dielectrics*. *Journal of the American Ceramic Society*, 30(4):114–125, 1947.

[50] S. Yamanaka, M. Fujikane, T. Hamaguchi, H. Muta, T. Oyama, T. Matsuda, S. Kobayashi, and K. Kurosaki. Thermophysical properties of $BaZrO_3$ and $BaCeO_3$. *Journal of Alloys and Compounds*, 359(12):109 – 113, 2003.

[51] K. Jacob and Y. Waseda. Potentiometric determination of the gibbs energies of formation of $SrZrO_3$ and $BaZrO_3$. *Metallurgical and Materials Transactions B*, 26(4):775–781, 1995.

[52] D. de Ligny and P. Richet. High-temperature heat capacity and thermal expansion of $srtio_3$ and $srzro_3$ perovskites. *Phys. Rev. B*, 53:3013–3022, Feb 1996.

[53] K. Itoh, K. Ochiai, H. Kawaguchi, C. Moriyoshia, and E. Nakamura. Structural fluctuations of $SrTiO_3$ in the cubic phase. *Ferroelectrics*, 159:85–90, 1994.

[54] F. W. Lytle. X-ray diffractometry of low-temperature phase transformations in strontium titanate. *J. Appl. Phys.*, 35(7):2212–2215, 1964.

[55] K.C. Goretta, E.T. Park, R.E. Koritala, M.M. Cuber, E.A. Pascual, N. Chen, A.R. de Arellano-Lpez, and J.L. Routbort. Thermomechanical response of polycrystalline $BaZrO_3$. *Physica C: Superconductivity*, 309(34):245 – 250, 1998.

[56] S. Devanarayanan and P. S. Narayanan. Thermal expansion of strontium titanate. *Indian Journal of Pure & Applied Physics*, 6:714–716, 1968.

[57] M. Guennou, P. Bouvier, J. Kreisel, and D. Machon. Pressure-temperature phase diagram of srtio$_3$ up to 53 GPa. *Phys. Rev. B*, 81:054115, Feb 2010.

[58] L.R. Edwards and R.W. Lynch. The high pressure compressibility and grneisen parameter of strontium titanate. *Journal of Physics and Chemistry of Solids*, 31(3):573 – 574, 1970.

[59] K.T. Jacob and G. Rajitha. Thermodynamic properties of strontium titanates: Sr_2TiO_4, $Sr_3Ti_2O_7$, $Sr_4Ti_3O_{10}$, and $SrTiO_3$. *The Journal of Chemical Thermodynamics*, 43(1):51 – 57, 2011.

[60] J. P. Coughlin and R. L. Orr. High temperature heat contents of meta- and orthotitanates of barium and strontium. *Journal of the American Chemical Society*, 75(3):530–531, 1953.

[61] H. Ledbetter, M. Lei, and S. Kim. Elastic constants, debye temperatures, and electron-phonon parameters of superconducting cuprates and related oxides. *Phase Transitions*, 23(1):61–70, 1990.

[62] E.H.P. Cordfunke and R.J.M. Konings. Thermochemical data for reactor materials and fission products, 1990.

[63] K.Nagarajan, R. Saha, R Babu, and C.K. Mathews. Thermodynamic functions of barium and strontium zirconates from calorimetric measurements. *Thermochimica Acta*, 90(0):297 – 304, 1985.

[64] S. Yamanaka, K. Kurosaki, T. Maekawa, T. Matsuda, S. Kobayashi, and M. Uno. Thermochemical and thermophysical properties of alkaline-earth perovskites. *Journal of Nuclear Materials*, 344(13):61 – 66, 2005.

[65] M. Ito and T. Matsuda. Thermoelectric properties of non-doped and y-doped $SrTiO_3$ polycrystals synthesized by polymerized complex process and hot pressing. *Journal of Alloys and Compounds*, 477(1-2):473 – 477, 2009.

[66] Z. Romanowski, P. Kempisty, J. Prywer, S. Krukowski, and A. Torzewska. Density Functional Theory Determination of Structural and Electronic Properties of Struvite. *The Journal of Physical Chemistry A*, 114(29):78007808, 2010.

Appendix A

LAMMPS Scripts

Some examples of LAMMPS input scripts for molecular dynamics simulation starting from experimental crystal structure at room temperature and ambient pressure.

Appendix B

List of Publications

International Peer-Reviewed Journals

- Goh, W. F., Yoon, T. L. and Khan, S. A., Molecular dynamics simulation of thermodynamic and thermal transport properties of strontium titanate with improved potential parameters, *Computational Materials Science*, **60** pp. 123 - 129, 2012.

- Goh, W. F., Khan, S. A. and Yoon, T. L., A molecular dynamics study of thermodynamic properties of barium zirconate, *Modelling and Simulation in Materials Science and Engineering*, **21** 045001, 2013.

Conference Proceedings

- Goh, W. F., Yoon, T. L. and Khan, S. A., Molecular dynamics simulation of thermal expansion and isothermal compressibility of strontium titanate, *2^{nd} Symposium of USM Fellowship 2011*, CABI Database, 2011.

- Goh, W. F., Khan, S. A. and Yoon, T. L., Molecular dynamics study of thermal expansion and isothermal compressibility of strontium titanate and barium zirconate, *National Physics Conference 2012*, AIP Conference Proceedings, 2012.

- Goh, W. F., Khan, S. A. and Yoon, T. L., A study of thermal properties of perovskite ceramic materials via molecular dynamics simulation, 4^{th} *International Conference on Solid State Science and Technology*, Journal of Solid State Science & Technology, 2012.